Acta Pharmaceutica Sinica B 2024;14(3):1362−1379

Chinese Pharmaceutical Association
Institute of Materia Medica, Chinese Academy of Medical Sciences

Acta Pharmaceutica Sinica B

www.elsevier.com/locate/apsb
www.sciencedirect.com

ORIGINAL ARTICLE

Engineered extracellular vesicles efficiently deliver CRISPR-Cas9 ribonucleoprotein (RNP) to inhibit herpes simplex virus1 infection *in vitro* and *in vivo*

Yuanda Wan[a], Liren Li[a,b], Ruilin Chen[a], Jiajia Han[a], Qiyun Lei[a], Zhipeng Chen[a], Xiaodong Tang[a], Wenyu Wu[c], Shuwen Liu[a,d,*], Xingang Yao[a,d,*]

[a]*NMPA Key Laboratory for Research and Evaluation of Drug Metabolism, Guangdong Provincial Key Laboratory of New Drug Screening, School of Pharmaceutical Sciences, Southern Medical University, Guangzhou 510515, China*
[b]*Center of Clinical Pharmacy, Nanfang Hospital, Southern Medical University, Guangzhou 510515, China*
[c]*State Key Laboratory of Ophthalmology, Zhongshan Ophthalmic Center, Sun Yat-sen University, Guangzhou 510060, China*
[d]*Key Laboratory of Infectious Diseases Research in South China (Southern Medical University), Ministry of Education, Guangzhou 510515, China*

Received 31 July 2023; received in revised form 26 September 2023; accepted 9 October 2023

KEY WORDS

Extracellular vesicles;
CRISPR/Cas9;
Ribonucleoproteins;
PTGFRN;
Fc/Spa;
HSV1;
Neuron-targeting;
Delivery

Abstract Extracellular vesicles (EVs) have recently emerged as a promising delivery platform for CRISPR/Cas9 ribonucleoproteins (RNPs), owing to their ability to minimize off-target effects and immune responses. However, enhancements are required to boost the efficiency and safety of Cas9 RNP enrichment within EVs. In response, we employed the Fc/Spa interaction system, in which the human Fc domain was fused to the intracellular domain of PTGFRN-Δ687 and anchored to the EV membrane. Simultaneously, the B domain of the Spa protein was fused to the C domain of cargos such as Cre or spCas9. Due to the robust interaction between Fc and Spa, this method enriched nearly twice the amount of cargo within the EVs. EVs loaded with spCas9 RNP targeting the HSV1 genome exhibited significant inhibition of viral replication *in vitro* and *in vivo*. Moreover, following neuron-targeting peptide RVG modification, the *in vivo* dosage in neural tissues substantially increased, contributing to the clearance of the HSV1 virus in neural tissues and exhibiting a lower off-target efficiency. These findings establish

*Corresponding authors.
E-mail addresses: yaoxingang@smu.edu.cn (Xingang Yao), liusw@smu.edu.cn (Shuwen Liu).

Peer review under the responsibility of Chinese Pharmaceutical Association and Institute of Materia Medica, Chinese Academy of Medical Sciences.

https://doi.org/10.1016/j.apsb.2023.10.004

a robust platform for efficient EV-based SpCas9 delivery, offering potential therapeutic advantages for HSV1 infections and other neurological disorders.

1. Introduction

Extracellular vesicles (EVs) are produced through the process of outward budding and fission of the plasma membrane or the fusion of multivesicular bodies with the plasma membrane[1]. These vesicles contain a complex array of components, including lipids, membrane and cytosolic proteins, and various types of nucleic acids such as microRNAs (miRNAs), RNA, and DNA. As a result of their composition, EVs have attracted significant interest and are currently widely used in drug delivery research[2].

CRISPR-Cas9 is a powerful genome-editing technology that has the potential to treat various diseases by directly modifying genomes. However, the most commonly used delivery vehicles for this purpose are viral systems, which can elicit immunogenic responses and are readily cleared by the complement system *in vivo*. Alternative strategies for the *in vivo* delivery of Cas9 are being explored to achieve more efficient and effective gene editing. An optimal approach for delivering Cas9 proteins or ribonucleoprotein complexes (RNPs) into target cells would involve directly introducing these agents into EVs. EVs have been widely used in CRISPR-Cas9 packaging and delivery in recent years[3]. Various molecules that anchor to EV membranes are commonly used to enrich specific cargos into EVs, such as platelet-derived growth factor receptor *N*-terminal domain transmembrane region (PDGFRN-TM, also known as the pDisplay system), prostaglandin F2 receptor negative regulator-Δ687 (PTGFRN-Δ687)[4], VSV-G-TM, lysosomal-associated membrane protein 2B (LAMP2B)[5], as well as CD63, CD8, and CD9[1]. Dooley and colleagues have pointed out that PTGFRN-Δ687 showed the best surface display efficiency compared to others[4]. Therefore, we applied PTGFRN-Δ687 in our system[4]. In our previous study, we modified CD63 and enriched the spCas9 RNP in EVs *via* the Com/Com system, which relies on the RNA-adaptor interaction, resulting a notable impact on gene editing[6]. However, it should be noted that Fc (human immunoglobulin fragment crystallizable) and SpA (Staphylococcal protein A) have a robust interaction. *Staphylococcus aureus* produces a 42 kDa factor, protein A (SpA), that contains five highly homologous extracellular Ig-binding domains in tandem, designated domains E, D, A, B, and C. The B domain of protein A is a three-helix, 59 residue module that binds the Fc-portion of IgGs with a K_d of about 10−50 nmol/L[7]; domain B was used for subsequent experiments (named Spa in this study for convenience). Since it is Spa derived from bacteria, it was fused to the *C*-terminal of *Streptococcus pyogenes* Cas9 (SpCas9) to reduce immunogenicity. Given the strong interaction between Fc/Spa and the high dissociation properties under acidic conditions, we hypothesize that this system could efficiently enrich target cargos into EVs produced by cells. Upon uptake by recipient cells, EVs can undergo effective dissociation upon changes in pH, ultimately releasing the cargo into the cytoplasm and exerting its function.

Herpes simplex virus (HSV), a highly prevalent human virus, has two subtypes: HSV-1 and HSV-2[8]. Currently, nucleoside anti-HSV drugs such as acyclovir and valacyclovir are utilized to manage symptoms and recurrence. However, these drugs have increasing adverse reactions and cross-resistance. After primary infection and productive replication in the corneal epithelium, HSV-1 retrogradely travels through ophthalmic nerves to the trigeminal ganglia, establishing a latent reservoir that persists throughout the individual's lifetime. Currently, no strategy can eradicate the existing virus. Addressing these challenges necessitates the elimination of HSV as a critical goal. To the best of our knowledge, several groups have applied CRISPR targeting the HSV genome to eliminate HSV infection. Adeno-associated virus system was used for HSV1-targeting endonuclease delivery in a mouse model, and it observed a clear elimination of HSV genomes and therapeutic efficacy[9,10]. Recently, another study designed a system to deliver the mRNA of SpCas9 targeting the *UL8* and *UL29* genes of HSV1, which packaged the sgRNAs with SpCas9 mRNA into a viral particle[11]. These results support the potential clinical utility of CRISPR-Cas9 for treating HSV infection. One drawback of the system is that it employs a lentivirus-based delivery strategy, which is prone to clearance by the immune system *in vivo* and lacks neurotargeting ability. Alternatively, using EV-based delivery systems has the potential to overcome these challenges.

This study presents a novel strategy for the enrichment of EVs based on the Fc/Spa system, resulting in effective cargo enrichment within EVs. The enrichment efficiency of three different EV membrane proteins was also compared through the Cre-LoxP system, and the PTGFRN-Δ687 was the most efficient. The effectiveness of this system was further evaluated in an HSV1 virus infection model *in vitro* and *in vivo*.

2. Materials and methods

2.1. Materials

The following reagents were obtained from various suppliers: RPIM1640 medium and DMEM medium were purchased from Thermo Fisher (MA, USA); FBS were purchased from Yeasen Biotech (Shanghai, China); Dil and DiO were purchased from Beyotime (Shanghai, China); LysoTracker and Pierce™ BCA Protein Assay Kit was purchased from Thermo Fisher (MA, USA); Puromycin was purchased from Avantor (Radnor, PA, USA); and restriction endonucleases, T4 Polynucleotide Kinase, and T4 DNA Ligase were purchased from NEB (Ipswich, MA, USA). The PMD™ 19-T Vector Cloning Kit and *E. coli* DH5α Competent Cells were obtained from TAKARA (Ōsaka) (Tokyo, Japan), and 293T cells were purchased from the National Collection of Authenticated Cell Cultures (Shanghai, China). The human alpha herpesvirus 1 strain F (HSV1) was a gift from Guangzhou Institutes of Biomedicine and Health.

Table 1 List of laboratory-constructed plasmids.

Plasmid	Primer (5'−3')	Primer (5'−3')	Restriction site	Result
pcDNA3.1a-Cre	CTAGCTAGCATGGGCCCAAA GAAGAAGAGAAAGG	CCGGAATTCCTAATCGCCATC TTCCAGCAGGC	NheI, EcoRI	Fig. S1C, Fig. 2E
pcDNA3.1a-Cre-Spa	CCGGAATTCGGATCCGGAGG AGGAGGAAG	CCGCTCGAGCTTGGGGGCCT GGCTCTCG	XhoI, EcoRI	Fig. 1D and E; Fig. 2
pDisplay-VSVG-TM	ccgTCCGGAgctctattgcctcttttttctttatc	ccgGAATTCctttccaagtcggttcatctctatg	BspEI, EcoRI	Fig. 1
pDisplay-VSVG-TM-Fc	GAATTCGGAGGAGGAGGCT CCGGAG	TCTAGACTACTTGTCATCGTCAT CCTTGTAG	EcoRI, XbaI	Fig. 1D and E
Lenti-PDGFRN-Fc-puro	GACACCGGTCTACTTGTCAT CGTCATCCTTGTAG	GACTTCGAAGGAGGAGGAGGC TCCGGA	AgeI, BstbI	Fig. 1D and E
pEnCMV-PTGFRNΔ687-Fc-flag	cctatatttaatgcttctgt	catggtggcGGTACCAAGCT	Circle PCR	Fig. 1D and E
pEnCMV-RVG-PTGFRN-Δ687-Fc-flag	CTAGCTAGCGGCACCATGG AGACAGACAC	TAAGGTACCTCCGGATGCGC CGCTGCCGCCGCC	NheI, KpnI	Fig. 5
Lenti-LoxP-red- LoxP-EGFP-puro	Digest by AgeI-SpeI from two vetors			Figs. 1 and 2

2.2. *Plasmid construction and sgRNA design*

All the plasmids used in this study were described in Table 1 and Table 2 pCAG-CRE-IRES2-GFP, pMSCV-LoxP-dsRed-LoxP-eGFP-Puro-WPRE, pEnCMV-PTGFRN-3 × Flag, LentiV2-SPA, pcDNA3.1a-VSV-G-TM, pCDNA3.1a-RVG-PDGFRN were constructed by GENWIZ (Suzhou, China). LentiCRISPRv2 puro was a gift from Brett Stringer (Addgene plasmid # 98290; http://n2t.net/addgene:98290; RRID: Addgene_98290)[12], psPAX2 was a gift from Didier Trono (Addgene plasmid # 12260; http://n2t.net/addgene:12260; RRID: Addgene_12260), pCAG-VSVG was a gift from Ian Wickersham (Addgene plasmid # 64084; http://n2t.net/addgene:64084; RRID: Addgene_64084). pcDNA3.1a-PDGFRN-TM, pcDNA3.1a-VSV-G-TM, pcDNA3.1a-PTGFRN-Δ687-TM, Lenti-CMV-LoxP-red-LoxP-EGFP, pcDNA3.1a-Cre, pcDNA3.1a-Cre-Spa plasmids were generated by this group. They will be made available upon request. All constructs generated were confirmed by Sanger sequencing from GENWIZ and Qingke company (Guangzhou, China). All the primers used in this study are described in Table 3.

2.3. *293T$^{LoxP\text{-}red\text{-}LoxP\text{-}EGFP}$ and 293T^{EGFP} reporter construct*

LoxP-red-LoxP-EGFP reporter cell was transiently transfected into 293T cells, named 293T $^{LoxP\text{-}red\text{-}LoxP\text{-}EGFP}$, and used for Cre activity validation. The 293T$^{LoxP\text{-}red\text{-}LoxP\text{-}EGFP}$ cells did not express EGFP due to the stop code in the frame of LoxP-red-LoxP. Once the LoxP-red-LoxP sequence was removed by Cre, the cell turned from red fluorescence to green fluorescence, and the number of GFP-positive cells was analyzed by fluorescence microscopy or flow cytometry (BD LSRFortessa X-20, NJ, USA). 293T^{EGFP} reporter cell was used for sgEGFP-Cas9 activity validation. Once in the presence of sgEGFP and SpCas9, the green fluorescence will weaken. The GFP signals were analyzed by fluorescence microscopy (Nikon, Tokyo, Japan) or flow cytometry (BD LSRFortessa X-20, NJ, USA).

2.4. *Production of engineered EVs*

Engineered EVs were produced by co-transfection of three plasmids into 293T cells: PTGFRN-Fc, VSV-G, and the target plasmid expressing Cre or SpCas9 with the respective gene-specific sgRNA. Briefly, 5 million actively proliferating 293T cells grown in 10-cm dishes were incubated with 10 mL of Opti-MEM (Thermo Fisher Scientific, MA, USA). 4.5 μg of PTGFRN or PTGFRN-Fc fusion protein-expressing plasmid, 3 μg of VSV-G, and 4.5 μg of target plasmid, such as SpCas9, SpCas9-Spa, Cre, or Cre-Spa, were used for engineered EVs production. In short, these plasmids were mixed in 0.5 mL of Opti-MEM. The amount of 36 μL of polyethyleneimine (PEI, Polysciences, Warrington, PA, USA) were mixed in 0.5 mL of Opti-MEM. These plasmids mixture and the PEI mixture were then mixed and incubated at room temperature for 15 min. The plasmid/PEI mixture was then added to the cells in Opti-MEM. Twenty-four hours after transfection, the medium was changed into 10 mL of Opti-MEM, and the Cas9 RNP-enriched EVs were collected 72 h after transfection.

2.5. *EVs isolation*

Ultracentrifugation was used to isolate EVs from the tissue culture medium following our published procedures[6]. Briefly, the cell culture medium was centrifuged at 200 × *g* for 10 min, 2000 × *g*

Table 2 List of plasmids purchased by the company.

Plasmid	Cat. No.	Company	Result
LentiV2-Spa	80-673395549-R1/A A29565-1/M575647	GENEWIZ	Fig. 3
pEnCMV-PTGFRN-3 × Flag	P24421	MiaoLing Plasmid Platform	Fig. 6
lentiCRISPRv2 puro	#98290	Addgene	Figs. 3−6
pCAG-VSVG	#64084		All Results
pCAG-CRE-IRES2-GFP	PM200	Ningbo Naisi Biotechnology	Figs. 1 and 2
pMSCV-loxp-dsRed-loxp-eGFP-Puro-WPRE	PM1104		

Table 3 List of primers used in this study.

Primer name	Forward primer (5′−3′)	Reverse primer (5′−3′)	Result
sgRNA-scaffold-R		GCACCGACTCGGTGCCACTT	Fig. 3F
sgRNA-EGFP	CACCGgagctggacggcgacgtaaa	AAACtttacgtcgccgtccagctcC	Fig. 3
sgRNA-UL8	CACCggacaccgcagatatcgtgt	AAACacacgatatctgcggtgtcc	Fig. 4A and B
sgRNA-UL29	caccGCGAGCGTACACGTATCCC	aaacGGGATACGTGTACGCTCGC	Figs. 4−6, Fig. S4
UL8-PCR	CGCCACAGAGTCGGGTTC	GGGGCGGTGAACTTTAGCA	Fig. 4B
UL29-PCR	CGTCAGTTTCAGGGACACCG	cacgcccccaggtaaagtgta	Figs. 4−6
gD gene	CCAAATACGCCTTAGCAGACC	CACAGTGATCGGGATGCTGG	Fig. 4E and 6F
VP16	AATGTGGTTTAGCTCCCGCA+	CCAGTTGGCGTGTCTGTTTC	Fig. 4E and 6F
GAPDH	TGACCTCAACTACATGGTCTACA	CTTCCCATTCTCGGCCTTG	All Results

for 10 min, and 12,000 × *g* for 30 min at 4 °C to remove cell debris (Eppendorf, 5425, Hamburg, Germany). The supernatant was centrifuged at 120,000 × *g* for 70 min at 4 °C. The pellet was washed once with PBS and centrifuged again under the same conditions. The resulting pellet containing the EVs was resuspended in PBS. Typically, EVs from 30 mL of supernatants were resuspended in 500 μL (60 × concentration) for *in vitro* and *in vivo* experiments.

2.6. *Particle size analysis of EVs*

Hydrodynamic diameters and concentrations of EVs were measured using the ZetaView (Particle Metrix, Ammersee, Germany), a nanoparticle tracking analysis (NTA) system to conduct extracellular concentration and size measurements of nanoparticles. This technique is based on the Brownian motion of individual particles and employs the Stokes−Einstein equation to calculate the hydrodynamic diameter and concentration of the nanoparticles. Subsequently, we also utilized an instrument based on the dynamic light scattering (DLS) principle to perform further testing for the polymer dispersity index (PDI) parameter. Concentrated samples containing EVs were serial diluted 1000-fold in cold PBS. Three independent measurements were obtained for each sample in triplicate. The diameter of the EV is the average of three measurements.

2.7. *Quantitation and degradation of SpCas9 in EVs*

The amount of 100 μL of EVs (1×10^{11} vesicles/mL) were added to293T cells in 24-well plates (2.5×10^4 cells/well). The cells cultured in Opti-MEM medium were incubated with EVs for 1, 8, 12, 24, 48, and 72 h, respectively. Then, these cells were washed three times with PBS buffer and lysed with SDS-lysis buffer for Western blotting assay. The standard SpCas9 protein (Z03389S, GenCrispr, Nanjing, China) was used for the semi-quantitation of packaged SpCas9 in EVs.

2.8. *Western blotting*

For Western blotting analysis, cell lysate or EVs (50 μL, 1×10^{11} vesicles/mL) were separated by SDS-PAGE and transferred to the PVDF membrane (Roche, Basel, Switzerland). After incubation with indicated primary antibodies overnight, the membranes were visualized using the Fluor Chem E System Dura detection system (Cleaver-Brooks, 92-14860-00, MN, USA). The primary antibodies used include gD antibody (ab6507), SpCas9 antibody (ab191468), TSG101 antibody (ab125011-10), which were purchased from Abcam Company, UK; GAPDH antibody (D4C6R), CD9 antibody (D801A), CD81 antibody (52892S), CD63 antibody (52090S), VSV-G antibody (E8S5G), Calnexin (CNX, C5C9) antibody were purchased from Cell Signaling Technology, Boston; PTGFRN antibody (Sino Biological, 101357-T32, Beijing, China), Flag antibody (F1804, Sigma), Cre antibody (Novagen, 69050-3, Merck KGaA, Darmstadt, Germany), HSV1 ICP8 antibody (10A3, SANTACRUZ) and anti-Rabbit IgG (H + L) (CST, 31460, Danvers, MA, USA) secondary antibodies were used in Western blotting. Densitometry (NIH ImageJ, Bethesda, MD, USA) was used to quantify protein amount.

2.9. *RNA isolation and RT-qPCR analysis*

To detect sgRNA in EVs, sgRNA (<200 bp) was purified from collected extracellular vehicles by miRNeasy Micro Kit (QIAGEN, 217084, Düsseldorf, Germany), which could collect RNA molecules from approximately >18 bp upwards. The PrimeScript™ IV strand cDNA Synthesis Mix (Takara, 6215A, Tokyo, Japan) was used to reverse-transcribe the RNA to cDNA. For EGFP sgRNA and UL29 sgRNA detection, sgRNA-EGFP-F, sgRNA-UL29-F, and sgRNA-scaffold were used as primers in SYBLGreen-based RT-qPCR individually. PCR was run on Roche LightCycler® 480. Primer information was included in Table 3. For sgRNA sequencing, the above PCR products were collected and inserted into the PMD 19-T vector using the cloning kit (Takara, 6013, Tokyo, Japan). Then, these clones were analyzed by Sanger sequencing after blue−white plaque screening.

2.10. *Transmission electron microscopy*

Transmission electron microscopy was performed at the Southern Medical University Central Laboratory. Collected EVs (about 1.0×10^{11} vehicles/mL) were stained with uranyl acetate. The particles were absorbed on plain carbon grids, dried, and observed under a Hitachi H-7650 electron microscope (HITACHI, Tokyo, Japan).

2.11. *T7 endonuclease I (T7EI) cleavage assay and TIDE analysis*

The genomic DNA (gDNA) was isolated using the Universal Genomic DNA Purification Mini Spin Kit (Beyotime, D0063, Shanghai, China). The resultant gDNA was used as a template for PCR with primers surrounding the sgRNA-UL8 and sgRNA-UL29 target sites. The following two pair primers were used for PCR amplification, named UL8-PCR-F, UL8-PCR-R, UL29-PCR-F, and UL29-PCR-R. Next, the PCR product was incubated with T7 Endonuclease I (T7EI) (NEB, M0302S, Ipswich, MA, USA)

according to the specification, and cleavage was visualized with an agarose gel (1.5%). DNA was then digested with 5−10 units of T7EI for 30−60 min at 37 °C and resolved in an agarose gel. Quantification of gene disruption was performed using ImageJ software (NIH49) and calculated using Eqs. (1) and (2):

$$\text{Mutant gene in the cell population (\%)} = 100 \times (1 - [1 - \text{Fraction cleaved}]1/2) \quad (1)$$

$$\text{Fraction cleaved} = \text{Density of cleaved product} / (\text{Density of cleaved product} + \text{Density of uncleaved product}) \quad (2)$$

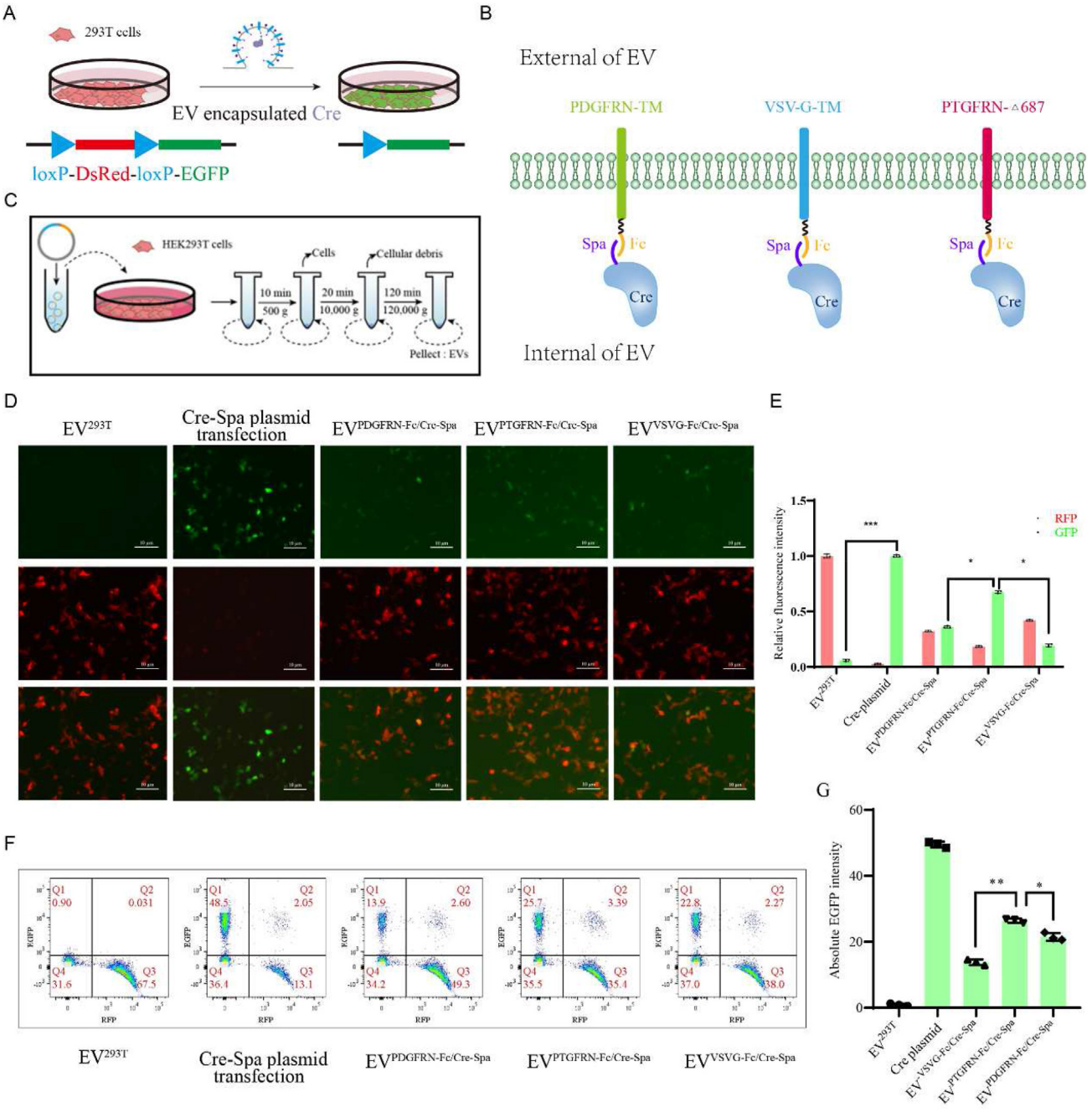

Figure 1 Evaluating the activity of engineered EVs by Cre/LoxP system. (A) Schematic diagram of the Cre-LoxP system for evaluating the efficiency of EV delivery. (B) The diagram of three designed engineered EVs with PDGFRN-TM-Fc, VSV-G-TM-Fc, or PTGFRN-Δ687-Fc, the Spa-B domain, was fused to the *C*-terminal of Cre. (C) The procedure of EVs collected from 293T cell supernatant. (D and E) The LoxP-red-LoxP-EGFP plasmid was transiently transfected into 293T cells. Cre-Spa plasmid transfection was a positive control. After 8 h, the cell supernatant was changed to the medium without EVs, and the indicated EVs (1×10^{10} vesicles) (EV^{293T}, $EV^{PDGFRN-Fc/Cre-Spa}$, $EV^{PTGFRN-Fc/Cre-Spa}$, and $EV^{VSVG-Fc/Cre-Spa}$) were added to the cells for incubation for 24 h. Scale bar = 100 μm. Then, the red and GFP signals were observed by fluorescence microscope (D and E) and flow cytometry (F and G). (E) The quantitation of fluorescence results. (F) The quantitation results of flow cytometry. Data were presented as mean ± SD ($n = 3$, $^*P < 0.05$, $^{**}P < 0.01$, $^{***}P < 0.001$).

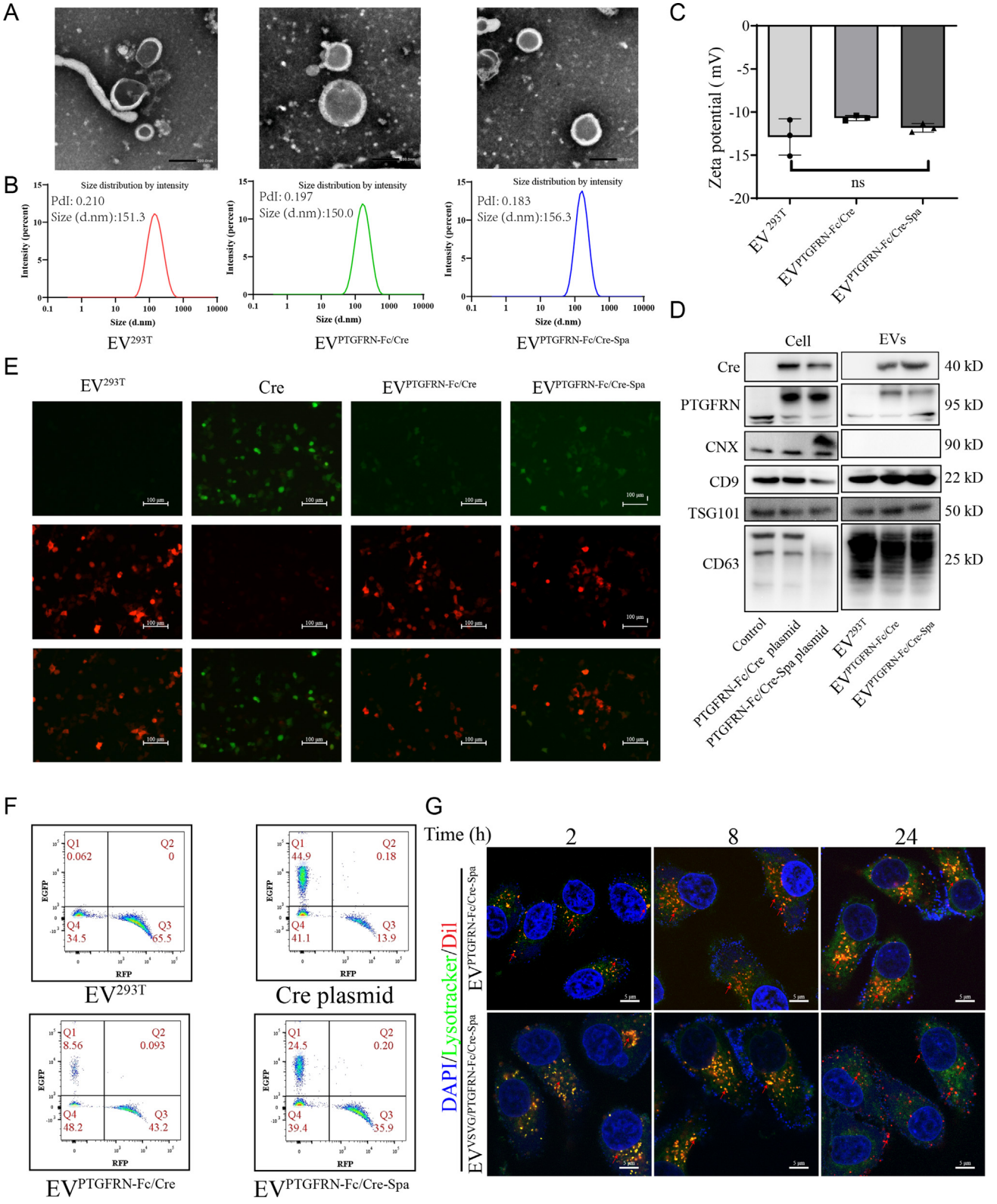

Figure 2 Characterization of engineered EVs. (A) The TEM (top panel) and (B) the diameter and PDI parameters of the isolated EVs, EV^{293T}, $EV^{PTGFRN-Fc/Cre}$ and $EV^{PTGFRN-Fc/Cre-Spa}$, scale bar = 200 nm. (C) Surface Zeta potential of EV^{293T}, $EV^{PTGFRN-Fc/Cre}$, and $EV^{PTGFRN-Fc/Cre-Spa}$. (D) The proteins in EVs (5×10^9 vesicles) and cell lysates were detected by Western blotting. (E and F) $293T^{LoxP}$ cells were incubated with EV^{293T}, $EV^{PTGFRN-Fc/Cre}$, and $EV^{PTGFRN-Fc/Cre-Spa}$ (1×10^{10} vesicles) for 24 h, then RFP and GFP signals were observed by (E) fluorescence microscope and (F) flow cytometry. Scale bar = 100 μm. (G) The EVs absorption by 293T was observed by confocal microscopy, scale bar = 100 μm. Lysosomes of 293T cells were labelled with lysotracker (green), indicated EVs were labelled with Dil (red), and the nucleus was stained with Hoechst as blue. The yellow color represented the colocalization of fluorescent signals from EVs and lysosomes. Scale bar = 5 μm. Data were presented as mean ± SD ($n = 3$, $^*P < 0.05$, $^{**}P < 0.01$, $^{***}P < 0.001$, *ns*, not significant).

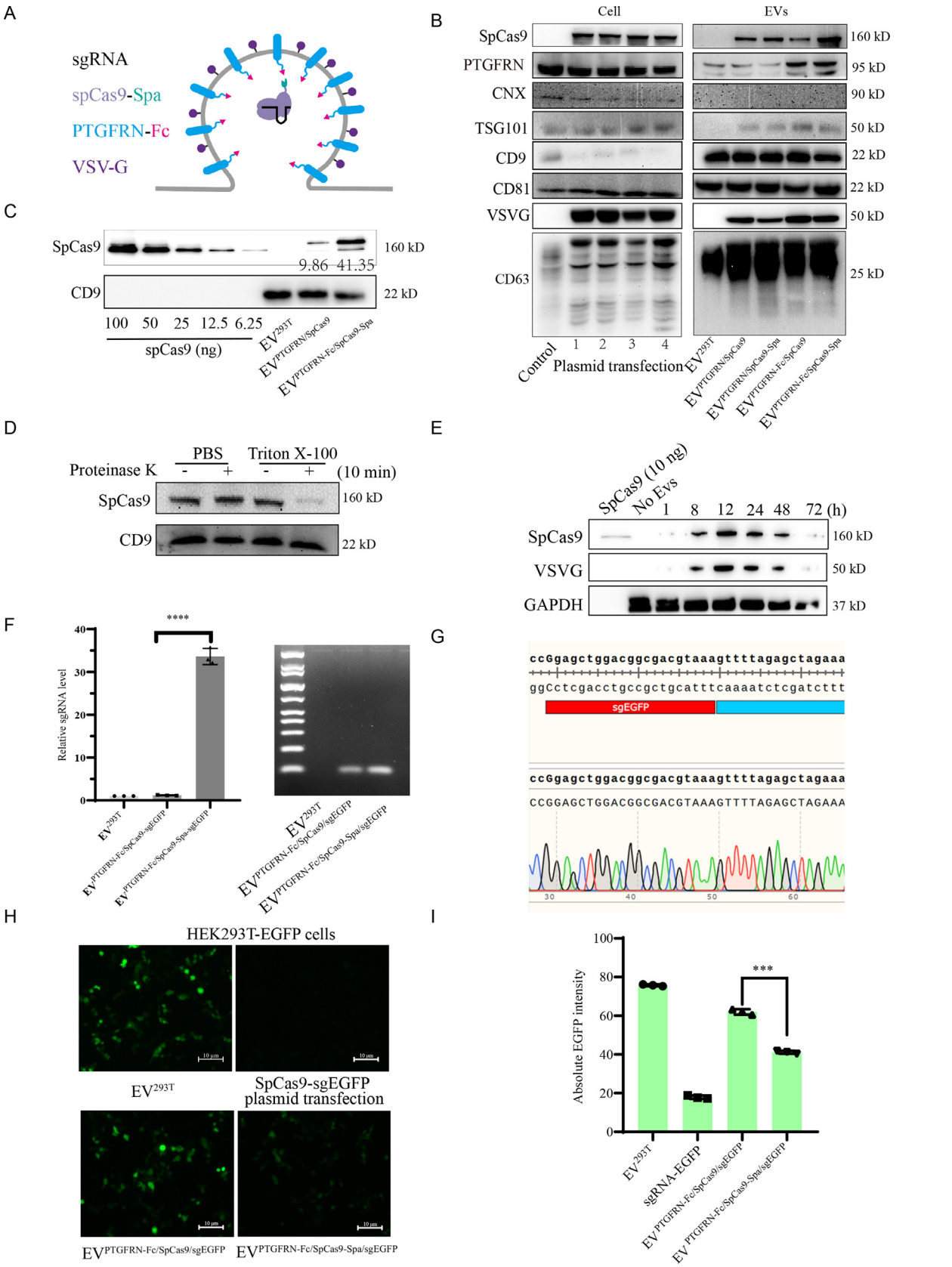

Figure 3 Fc/Spa system enriched SpCas9 into EVs. (A) Schematic illustration of the enrichment of SpCas9 into EV. (B) The proteins in EVs (5×10^9 vesicles) and cell lysates were detected by Western blotting. 1: PTGFRN and spCas9 plasmids transfection; 2: PTGFRN and spCas9-Spa plasmids transfection; 3: PTGFRN-Fc and spCas9-Spa plasmids transfection; 4: PTGFRN-Fc and spCas9-Spa plasmids transfection. (C) SpCas9 in EVs was detected semi-quantitatively by Western blotting. (D) $EV^{PTGFRN-Fc/SpCas9-Spa}$ were treated with/without 0.25% Triton X-100 and with/without

These PCR products were also sequenced by Sanger sequencing and analyzed by Tracking of Indels by Decomposition (TIDE) (https://tide.nki.nl/).

2.12. Proteinase K and RNase a protection assays

EVs derived from cells overexpressing spCas9/sgRNA-EGFP were isolated, as described above. Equal volumes (25 μL, 1×10^{10} vesicles/mL) of EVs were treated with or without proteinase K (0.5 μg/mL) and with or without 0.25% Triton X-100 and incubated at 37 °C for 30 min. Levels of spCas9 in EVs were analyzed by Western blotting. For determining sgRNA content, the digestion mixture was stopped by the addition of an RNA column purification reagent and then subject to RT-qPCR as described above using the following primers: sgRNA-EGFP forward primer: 5′GATCGGAGCTGGACGGCG ACGTAAAG3′. sgRNA-scaffold reverse primer 5′GCACCGACTC GGTGCCACTT3′.

2.13. Off-target detection and next-generation sequencing

The off-target of sgRNA was analyzed by Off-Spotter (https://cm.jefferson.edu/Off-Spotter/) and Cas-OFFinder (http://www.rgenome.net/cas-offinder/), the two tolls give similar results. Then, these predicted mismatch genes were analyzed by next-generation sequencing. The DNA region containing the target sequences was amplified by the 2 × PCR Mix (Dye Plus) from Vazyme, Nanjing, China. The purified PCR products were analyzed by next-generation sequencing by GENEWIZ. Analysis of insertions and deletions (INDEL) was done with the online CRISPRESSO2[13]. PCR primers used for amplifying each target sequence are listed in Table 3.

2.14. Cellular toxicity assay

293T, Vero, and Hela cells were plated into 96-well plates (5×10^3 cells/well). The above EVs were diluted into concentration gradients and then added to the cells and cultured for 24 h. Ten microliters of 0.5% solution of 3-[4,5-dimethylthiazole-2-yl]-2,5-diphenyltetrazolium ammonium bromide (MTT) was added to each well. Subsequently, after 4 h, the supernatant was aspirated, and DMSO was added to dissolve MTT. The absorbance of each well was then measured at 570 nm using a microplate reader (Tecan, Männedorf Switzerland), and the relative cell viability was calculated.

2.15. CPE assay

Based on our previous report[14–16], Vero cells were cultured in 24-well plates (1×10^4 cells/well) overnight. Then, the indicated plasmids were transfected into these cells. Before the HSV1 virus infection, the serum-containing medium was discarded, and the cells were washed twice with PBS. Then, the virus was diluted with DMEM medium without fetal bovine serum and inoculated with Vero cells for 1 h at 37 °C. The virus was removed, and the indicated EVs were added into the 2% DMEM medium without EVs as a maintained culture. After about 48 h, cellular CPE was observed under a microscope (Nikon, Tokyo, Japan).

2.16. Plaque formation assay

Vero cells were cultured in a 12-well plate (2.5×10^5 cells/well) overnight[17]. The supernatant containing the progeny virus was added into the Vero cells and incubated at 37 °C for 1 h and was maintained with a maintenance medium containing 1.6% methylcellulose for nearly 24–36 h until the lesions were visible under a microscope. Next, these cells were fixed with 4% paraformaldehyde and stained with crystal violet (Macklin, C805211, Shanghai, China) for 30 min, then washed and photographed by microscope.

2.17. Quantitative real-time PCR (RT-qPCR)

Mouse tissue RNA was extracted using the Animal Total RNA Isolation Kit (Macklin, C805211, Shanghai, China), and cellular RNA was extracted using the Animal Total RNA Isolation Kit (Foregene, RE-03113, Chengdu, China). The reverse-transcribed cDNA was subjected to real-time PCR using PrimeScript™ RT Master Mix (RR036Q, Takara). PCR primers used for amplifying each target sequence are listed in Table 3.

2.18. Cellular uptake assay

EVs were labelled with Dil before the supernatant was collected for ultracentrifugation. Dil (0.1 mg/mL) was added into the supernatant and incubated at 37 °C for 20 min. The subsequent steps were the same as those for ultracentrifugation. Then, the EVs were incubated with the cells flowing labelled with LysoTracker at 37 °C for 5 min. At the indicated time, the cells were fixed with 4% paraformaldehyde, and the nucleus was stained with Hoechst 33342 (Yeasen, 40731ES10, Shanghai, China). In the end, the cells were observed under a confocal microscope (LSM 880, Carl Zeiss, Oberkochen, Germany).

2.19. Transwell assay

HUVEC cells and HT22 cells were used to generate an *in vitro* EV penetration model. HUVEC cells (1×10^5 cells/well) were plated on the top side of 0.4-μm pore size Transwell membrane (24-mm Transwell™, Corning, NY, USA), which were pre-coated with gelatin first. HT22 (5×10^4 cells/well) were cultured in the lower chamber. After the *trans*-endothelial electrical resistance (TEER) of this model reached 150 Ω cm^2, Dil-labelled EVs in fresh culture media were added to the top chamber. HUVEC cells (the cell membrane was stained with DiO), HT22 cells (the nuclei were stained with Hoechst 33342) as well as XZ images of the Transwell models, were individually captured by CLSM (Nikon, Tokyo, Japan) at 24 h incubation.

proteinase K (0.5 μg/mL) for 30 min. Expression levels of SpCas9 and CD9 were determined by Western blotting. (E) $EV^{PTGFRN-Fc/SpCas9-Spa}$ were added into 293T cells and incubated for 1, 8, 12, 24, 48 or 72 h, respectively. Expression levels of spCas9, VSVG, and GAPDH were analyzed by Western blotting. (F) The total micro RNAs in EVs (1×10^{10} vesicles) were extracted, and RT-PCR was performed to detect the level of sgRNA-EGFP. The RT-PCR results were shown on the left, and the agarose electrophoresis results were shown on the right. (G) The Sanger sequence of sgRNA-EGFP from (F). (H and I) $293T^{EGFP}$ cells were incubated with $EV^{PTGFRN-Fc/SpCas9/sgEGFP}$ for 48 h, and then the EGFP signal was observed by fluorescence microscope (H) and flow cytometry (I). Scale bars, 100 μm. Data were presented as mean ± SD ($n = 3$, $^{***}P < 0.001$).

2.20. *In vivo biodistribution and pharmacokinetic characteristics of EVs*

The mice were intravenously injected with Dil-labelled EV^{293T}, $EV^{PTGFRN-Fc/SpCas9-Spa/sgUL29}$ and $EV^{RVG-PTGFRN-Fc/SpCas9-Spa/sgUL29}$ (10^{10} particles/mice). At 12 h after injection, the BALB/c mice ($n = 6$, male) were anesthetized, and the Dil fluorescence signal imaging of mice organs (brain, heart, liver, spleen, lung, and kidney) was visualized by *In Vivo* Imaging Systems (Beckman Coulter, IN, USA) for the *in vivo* biodistribution. To

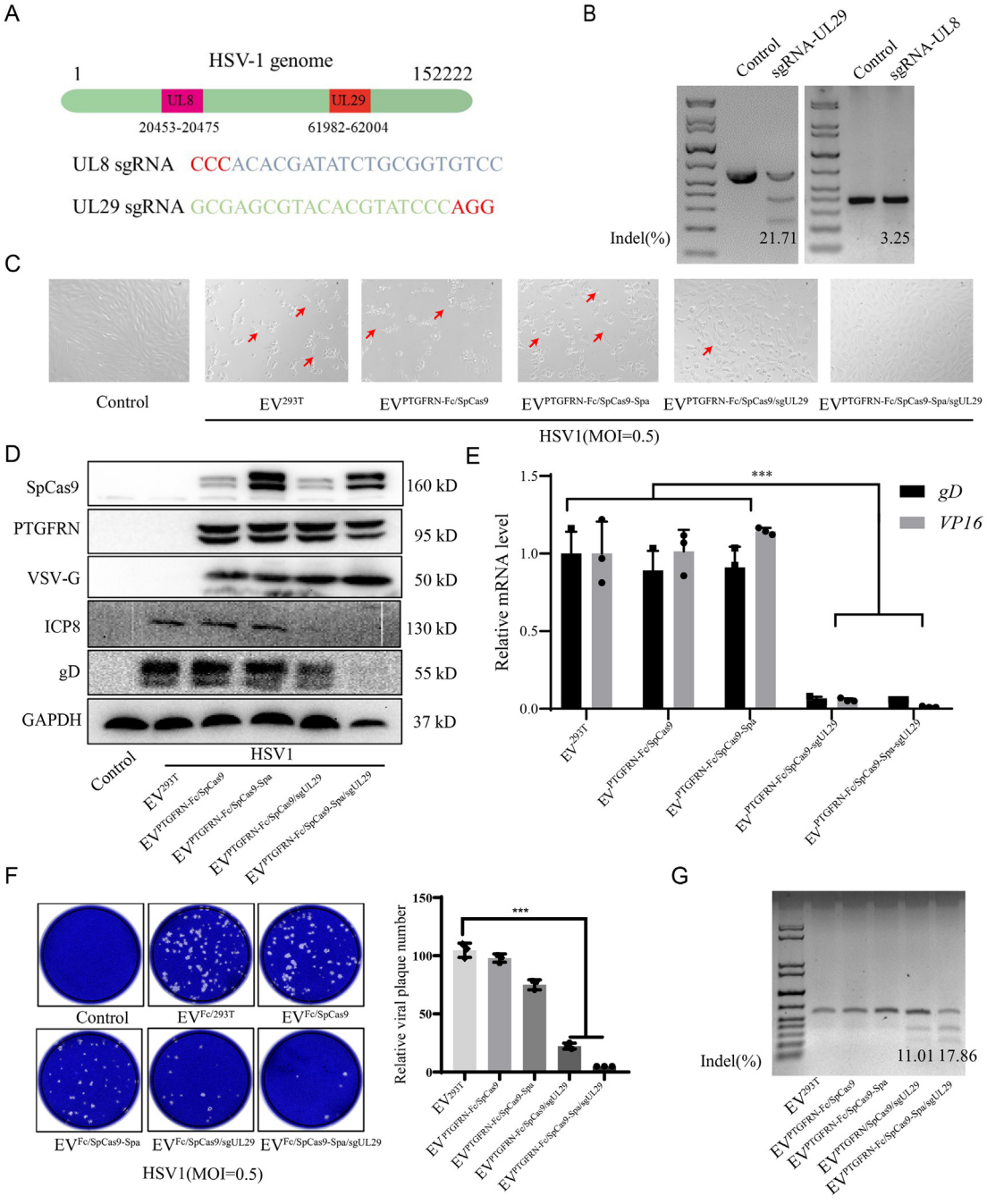

Figure 4 The design of EVs against HSV1. (A) The schematic diagram of the HSV1 genome, $sgRNA^{UL8}$ targeting the glycoprotein UL8 and $sgRNA^{UL29}$ targeting single-stranded DNA binding protein UL29 (protein name: ICP8). (B) The gene editing efficiency of $sgRNA^{UL8}$ and $sgRNA^{UL29}$ was detected by T7EI. The sgRNA-UL8 and sgRNA-UL29 were transited and infected with HSV-1 in Hela cells as the experimental group, and Hela cells were only infected with HSV-1 as the blank control. (C–G) Vero cell was infected with HSV1 for 1 h, then EV^{293T}, $EV^{PTGFRN-Fc/SpCas9}$, $EV^{PTGFRN-Fc/SpCas9-Spa}$, $EV^{PTGFRN-Fc/SpCas9/sgUL29}$ and $EV^{PTGFRN-Fc/SpCas9-Spa/sgUL29}$ (1×10^{10} vesicles) were added for 48 h. (C) The CPE results were observed under the microscope. (D) The viral protein levels were analyzed by Western blotting. (E) The gene transcriptional levels of *gD* and *VP16* were analyzed by RT-qPCR. (F) The plaque assay was observed under the microscope. The histogram is a quantification of the viral plaque. (G) The gene editing efficiency was detected by T7EI. Data were presented as mean ± SD ($n = 3$, $^{***}P < 0.001$).

evaluate the pharmacokinetic characteristics of EVs, EVs were slowly injected intravenously into BALB/c mice (male) ($n = 3$). After injection, the serum was collected from the BALB/c mice at different time points (1, 2, 4, 12, 24, 48, or 72 h) and detected Dil signal using a microplate reader (Ex/Em: 549/600 ± 20 nm). The pharmacokinetic characteristics were shown by curves.

2.21. Antiviral assay in vivo

All experimental procedures were executed according to the protocols approved by the Institutional Animal Care and Use Committee of the Southern Medical University. BALB/c mice (males) from Southern Medical University were maintained under 12 h light−12 h dark conditions throughout, with food and water continuously available, and were weighed daily. Intranasal infection of BALB/c mice was performed as previously described[18]. Stocks of HSV1 were produced by Vero cells, and supernatants were aliquoted and frozen. The virus was diluted to 1×10^7 PFU/mL with serum-free DMEM. Mice ($n = 6$) received 20 μL of either stock into each nostril while anesthetized by isoflurane inhalation (2.5%−5.0%). The male mice were assigned randomly to experimental and control groups. These mice were then injected with 100 μL (1×10^{10} vesicles/mL) of indicated EVs *via* the tail vein for 7 consecutive days, and the control mice were injected with the same volume of PBS. Mice's behaviour and death were monitored every day. After 15 days, all mice were CO_2 euthanized, and the tissues were isolated for further analysis. Kaplan−Meier plots of mouse survival were prepared using a log-rank Mantel-Cox test.

2.22. Hematoxylin and eosin stain (HE stain)

After mice tissues had been collected and fixed, they were embedded in melted paraffin wax. The resulting block was mounted on a microtome and cut into 5-μm thick slices. The slices were affixed to microscope slides, at which point the wax was removed with a solvent, and the tissue slices attached to the slides were rehydrated and ready for staining. Hematoxylin principally colors the nuclei of cells blue. The cytoplasm was eosinophilic and was rendered pink-stained by eosin. The slices were observed under a microscope.

2.23. RVG antibody detection by ELISA

We detected the presence of antibodies to the RVG, and serum was collected from the mice on Day 8 and was diluted at 1:100 and 1:1000. The synthesized RVG peptide (29 aa) was immobilized onto a 96-well plate (Thermo Fisher Scientific, 436006, MA, USA), and the bound antibody was detected with a goat anti-mouse Ig-HRP conjugate (CST, 7076S, Danvers, MA, USA). Enzyme-linked immunosorbent assay (ELISA) was developed using substrate TMB. After the substrate was added, a reaction occurred with the target substance, resulting in a color change. The intensity of this color was then measured using a microreader at a wavelength of 450 nm. This allowed for the quantification and detection of the substance being studied.

2.24. Mice behavioural test

Open field test is a commonly used behavioural test in preclinical research to assess exploratory behaviour, locomotor activity, and anxiety-like behaviour in animal models[19]. Mice were placed in the corner of a plastic box (36 cm × 29 cm × 23 cm) with the base divided into equal sectors for a 5-min acclimation period. Subsequently, the map, total distance, and ambulatory episode average velocity were recorded for 5 min. A novel object recognition test is a behavioural test commonly used in preclinical research to assess recognition memory in animal models[20]. The test consisted of three sessions. On the first day, the mice were allowed to freely explore the box in the absence of any object for 5 min. On the second day, they were allowed to explore two identical objects for 5 min. On the third day, one of the objects was replaced by a novel object with a different shape and color, and the mice were allowed to explore the box for 5 min. The recognition index (RI) was calculated by dividing the amount of time spent exploring any one of the two objects or the novel object by the total time spent exploring both objects. The Rotarod test is a common method to assess neuromuscular coordination[21]. First, mice were positioned on a rotating rod (6 cm diameter) for 30 s and then trained at a constant speed of 12 rpm for 180 s (Nolei Xinda, YLS-31A, Tianjin, China). Sixty minutes after the last training, a mouse was placed on the rod, and the incubation period of its fall was recorded as the endpoint measurement. The average time of three trials was calculated for statistical analysis.

2.25. Statistical analysis

GraphPad Prism software free trail (Prism 5, Boston, MA, USA) was used for statistical analyses. In all cases, parametric or nonparametric tests and the appropriate post hoc test were applied. If data conformed to the normality and equivariance (parametric) of the analysis of variance (ANOVA) hypothesis, a one-way ANOVA was performed, followed by a Holm−Sidak multiple comparison post hoc test. Instead, multiple comparisons were performed by a Kruskal−Wallis one-way ANOVA on ranks followed by Dunnett multiple comparisons post hoc test for the data that did not meet ANOVA assumptions (nonparametric). In addition, the Student's *t*-test was conducted for some cases. All the data are expressed as the Mean ± standard deviation (SD). $P < 0.05$ was regarded as statistically significant. $^*P < 0.05$, $^{**}P < 0.01$, $^{***}P < 0.001$.

3. Results

3.1. PTGFRN-Δ687 mediated Fc-Spa system demonstrates EV cargo-loading capacity

Three types of EV membrane proteins, namely PDGFRN-TM, VSV-G-TM, and PTGFRN-Δ687, have been identified as effective for encapsulating target proteins into EVs. However, the cargo delivery efficiency of these systems is not uniform and varies depending on the specific system used. It is desirable to compare the efficiencies of these systems under identical conditions. For this purpose, we developed a Cre-LoxP reporter system, as recently reported[22], in which the plasmid with LoxP-red-LoxP-EGFP sequence was transfected into 293T cells ($293T^{LoxP}$). EVs can deliver Cre protein to $293T^{LoxP}$ cells, resulting in a shift from red to green fluorescence signal (Fig. 1A), which can be observed and measured using fluorescence microscopy and flow cytometry. The effectiveness of the EV-anchoring membrane proteins in cargo delivery can be evaluated by monitoring the change in green fluorescence. Human Fc was fused to the intracellular domain of EV-anchoring proteins, such as

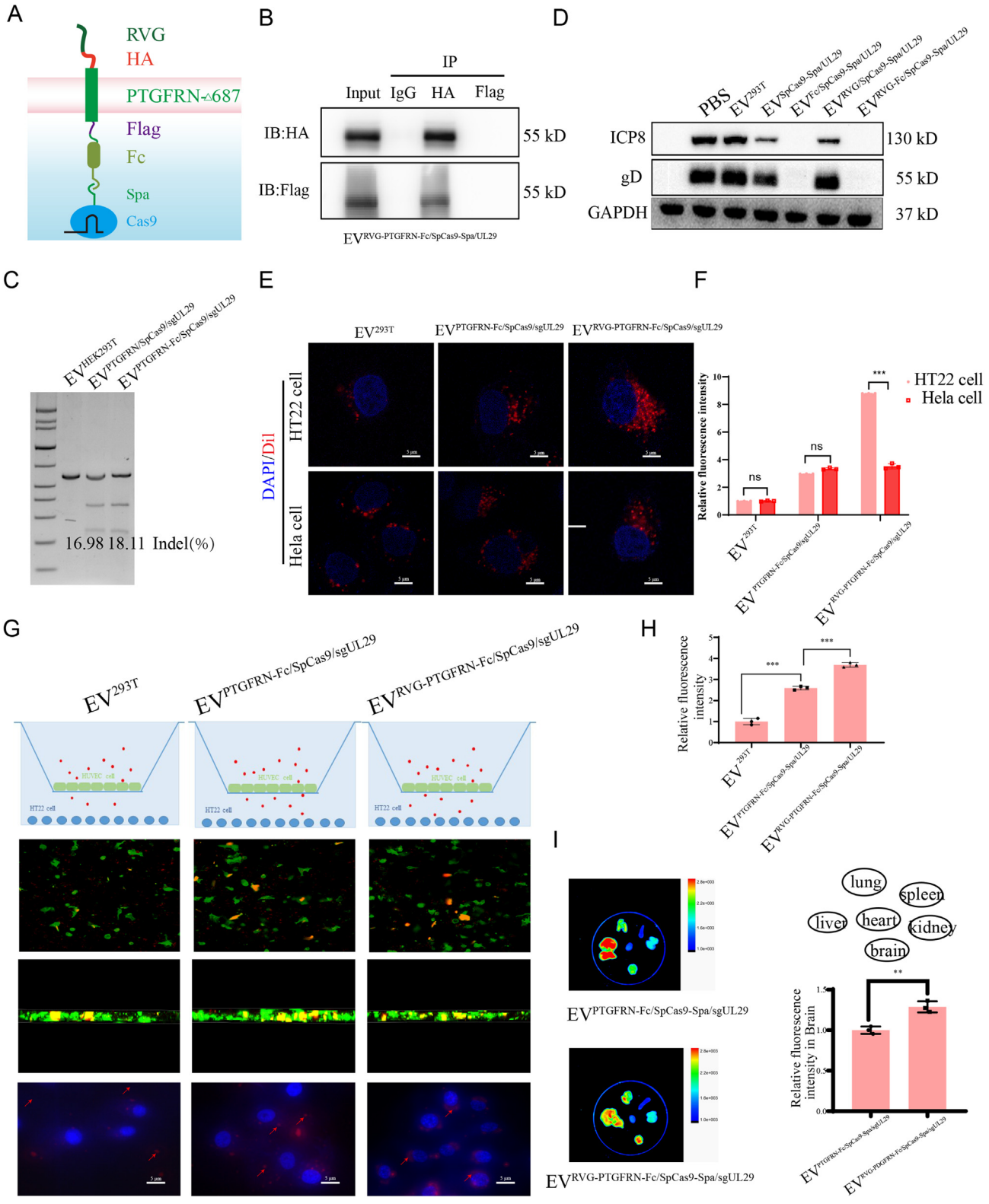

Figure 5 Neuro-targeting of EV mediated by RVG. (A) The schematic diagram of RVG-decorated $EV^{RVG-PTGFRN-Fc/SpCas9/sgUL29}$. (B) Western blots of $EV^{RVG-PTGFRN-Fc/SpCas9/sgUL29}$ after EV pulldown with either anti-HA or anti-FLAG beads. Anti-HA beads retain HA-EVs better than anti-HA beads retain HA-EVs. (C) The gene editing efficiency between $EV^{PTGFRN-Fc/SpCas9-Spa/sgUL29}$ and $EV^{RVG-PTGFRN-Fc/SpCas9-Spa/sgUL29}$ was analyzed by T7EI assay. After Hela cells were infected with HSV-1 for 1 h, EV^{293T}, $EV^{PTGFRN-Fc/SpCas9-Spa/sgUL29}$, and $EV^{RVG-PTGFRN-Fc/SpCas9-Spa/sgUL2}$ (1×10^{10} vesicles) were added, respectively, genomic DNA was extracted, and PCR was performed after 24 h. (D) The effects of indicated EVs on viral ICP8 and gD protein were evaluated by Western blotting. (E) Hela cells and HT22 cells were incubated with Dil-labelled

PDGFRN-TM, VSV-G-TM or PTGFRN-Δ687 (Fig. 1B). While the Spa[7] was fused to the *C*-terminal domain of Cre, named Cre-Spa (Fig. 1B). The transient transfection of the Cre-Spa plasmid into $293T^{LoxP}$ cell indicated the modification did not affect the function of Cre to cut LoxP site (Supporting Information Fig. S1A–D). Then, these plasmids were transfected into 293T cells to produce engineered EVs, named $EV^{PDGFRN-Fc/Cre-Spa}$, $EV^{VSVG-Fc/Cre-Spa}$, and $EV^{PTGFRN-Fc/Cre-Spa}$ (PTGFRN-Δ687 was abbreviated as PTGFRN for convenience in the flowing), respectively. These EVs were isolated by ultracentrifugation according to MISEV (2017) standard procedures as our previous report[23] (Fig. 1C). Immediately, these EVs were incubated with $293T^{LoxP}$ cells and the green fluorescence cell ratio was quantified by fluorescence microscopy (Fig. 1D and E) and flow cytometry (Fig. 1F and G). The result indicated that $EV^{PTGFRN-Fc/Cre-Spa}$ showed the highest green fluorescence signal (25.7% by flow cytometry), which demonstrated that PTGFRN-Δ687-based Fc could encapsulate more Cre into EVs through the interaction between Spa and Fc. Therefore, we adopted this system in the follow-up study.

Then, we studied the characteristics of EVs between 293T cell-derived EVs (EV^{293T}), $EV^{PTGFRN-Fc/Cre}$, and $EV^{PTGFRN-Fc/Cre-Spa}$. Transmission electron microscopy (TEM) results showed that these modifications did not affect the overall shape between EV^{293T} and $EV^{PTGFRN-Fc/Cre}$ or $EV^{PTGFRN-Fc/Cre-Spa}$ (Fig. 2A). Also, the quantity and size of EVs were similar between EV^{293T}, $EV^{PTGFRN-Fc/Cre}$ or $EV^{PTGFRN-Fc/Cre-Spa}$ from nanoparticle tracking analysis (NTA) and dynamic light scattering (DLS), we got about 10^{11} EVs from 10^7 cells, and about one cell produced 10^4 EVs. From the diameter data through NTA, it can be observed that the overall size is around ∼150 nm, as polymer dispersity index (PDI) data is consistently around ∼0.2 from DLS (Fig. 2B). There was no difference in the Zeta potentials between EV^{293T} and $EV^{PTGFRN-Fc/Cre}$ or $EV^{PTGFRN-Fc/Cre-Spa}$, which indicated that EVs stability in solution was not affected by engineering (Fig. 2C). Compared with EVs from 293T cells themselves, these modifications did not affect the biomarkers of EVs *via* Western blotting results, such as CD63, CD9 and TSG101 (Fig. 2D). CNX was used as a negative control. Notably, the Fc/Spa system increased the Cre content in $EV^{PTGFRN-Fc/Cre-Spa}$ compared with $EV^{PTGFRN-Fc/Cre}$ (Fig. 2D). To confirm the specificity of Spa/Fc, we compared the green fluorescence signal between $EV^{PTGFRN-Fc/Cre-Spa}$ and $EV^{PTGFRN-Fc/Cre}$ treatment, it has indicated a 3-fold fluoresce increase by $EV^{PTGFRN-Fc/Cre-Spa}$ treatment in $293T^{LoxP}$ by flow cytometry (8.54% *vs.* 24.5%) (Fig. 2E and F).

Based on our earlier discovery of the critical role of VSV-G in EV delivery, we thought that VSV-G might contribute to the lysosomal escape of cargos[24], which could undergo a low-pH-induced conformational change, becoming fusion-competent and enabling fusion between the viral membrane and the endosomal/lysosomal membranes[25]. So, we compared the intracellular kinetic behaviour of $EV^{VSVG/PTGFRN-Fc/Cre-Spa}$ or $EV^{PTGFRN-Fc/Cre-Spa}$ using confocal fluorescence microscopy. As shown in Fig. 2G, for $EV^{PTGFRN-Fc/Cre-Spa}$ and $EV^{VSVG/PTGFRN-Fc/Cre-Spa}$, by using fluorescent dye Dil (red) to label EVs and a LysoTracker-Green dye (green) to label lysosomes, we observed that at the 2 h incubation, EVs partially co-localized with the lysosomes, which appear as yellow spots. After 8 h, they completely co-localized, suggesting that the EVs had successfully entered the lysosomes (Fig. 2G). After incubating for 24 h, the analysis showed a decrease in yellow fluorescence and an increase in red fluorescence in the $EV^{VSVG/PTGFRN-Fc/Cre-Spa}$ group, suggesting successful lysosomal escape of the EVs. However, $EV^{PTGFRN-Fc/Cre-Spa}$ was still co-localized with the endosome (Fig. 2G). Moreover, we used ImageJ software to ascertain the Pearson correlation coefficient between lysosomes and EVs, which is changed from 0.73 to 0.85 to 0.15 with the indicated time, indicating a good dissociation of $EV^{VSVG/PTGFRN-Fc/Cre-Spa}$. These findings indicated the lysosomal escape ability of VSV-G, leading to its usage in subsequent studies. The Fc/Spa interaction system is acid-sensitive and reversible. To further verify this reversible process, we experimented with using chloroquine to inhibit endosome acidification during EV endocytosis. We found that the addition of chloroquine significantly reduced the ability of $EV^{PTGFRN-Fc/Cre-Spa}$ to enhance EGFP fluorescence on $293T^{LoxP}$ cells compared to the group without chloroquine incubation (Fig. S1E and 1F). This result demonstrated the Fc/Spa interaction system was acid-sensitive and reversible, emphasizing the crucial role of intracellular acidification in the dissociation of Fc/Spa. The PTGFRN-Fc/Spa system not only effectively packaged targeted cargos into EVs but also allowed for lysosomal clearance avoidance and intact cytoplasmic delivery into recipient cells. This system was thus employed for CRISPR-SpCas9 delivery in subsequent experiments.

3.2. *Efficient encapsulation of Cas9/sgRNA-RNP into EVs by Fc/Spa system*

We proceeded to determine if the Fc/Spa system exhibited a preference for encapsulating SpCas9 into EVs in 293T cells (Fig. 3A). Spa was fused to the *C*-terminal of SpCas9 protein named SpCas9-Spa. The transfected plasmids were used to generate engineered EVs by 293T cells, which were then named EV^{293T}, $EV^{PTGFRN-Fc/SpCas9}$, and $EV^{PTGFRN-Fc/SpCas9-Spa}$. Ultracentrifugation was employed to isolate EVs, as depicted in Fig. 1C. The characteristics of EVs were analyzed, and they exhibited the anticipated cup-like structure with a similar size and Zeta potentials (Supporting Information Fig. S2A and B). The features of EVs were validated through the presence of beneficial EV protein markers (TSG101, CD9, CD81, and CD63) and the lack of calnexin (Fig. 3B). This data suggested that the level of SpCas9 encapsulated within $EV^{PTGFRN-Fc/SpCas9-Spa}$ was approximately twice as high as that within $EV^{PTGFRN-Fc/SpCas9}$ we adopted a semi-quantitative approach by Western blotting as previously reported[6]. The results showed that the ability of Spa/Fc to promote SpCas9 protein packaging was nearly 4 times that of natural

EVs (2.5×10^9 vesicles) (Red) for 12 h. Then, the red fluoresce was observed under a microscope, scale bar = 5 μm. (F) The quantitation of (E). (G) The ability of blood vessels penetration of EVs, scale bar = 5 μm. EVs (2.5×10^9 vesicles) (EV^{293T}, $EV^{PTGFRN-Fc/SpCas9-Spa/sgUL29}$ and $EV^{RVG-PTGFRN-Fc/SpCas9-Spa/sgUL29}$) were added to the up Transwell chamber for 12 h, then fluorescence changes in the Transwell were observed under a fluorescence microscope. Red: EV marked by Dil; Blue: Hoechst labelled nucleus; Green: HUVEC cells labelled with DiO. (H) The quantitation of (G). (I) *In vivo* distribution of Dil-labelled EVs in mouse organs. Heart, liver, spleen, lung, kidney and brain. Data were presented as mean ± SD ($n = 3$, $^*P < 0.05$, $^{**}P < 0.01$, $^{***}P < 0.001$, ns, not significant).

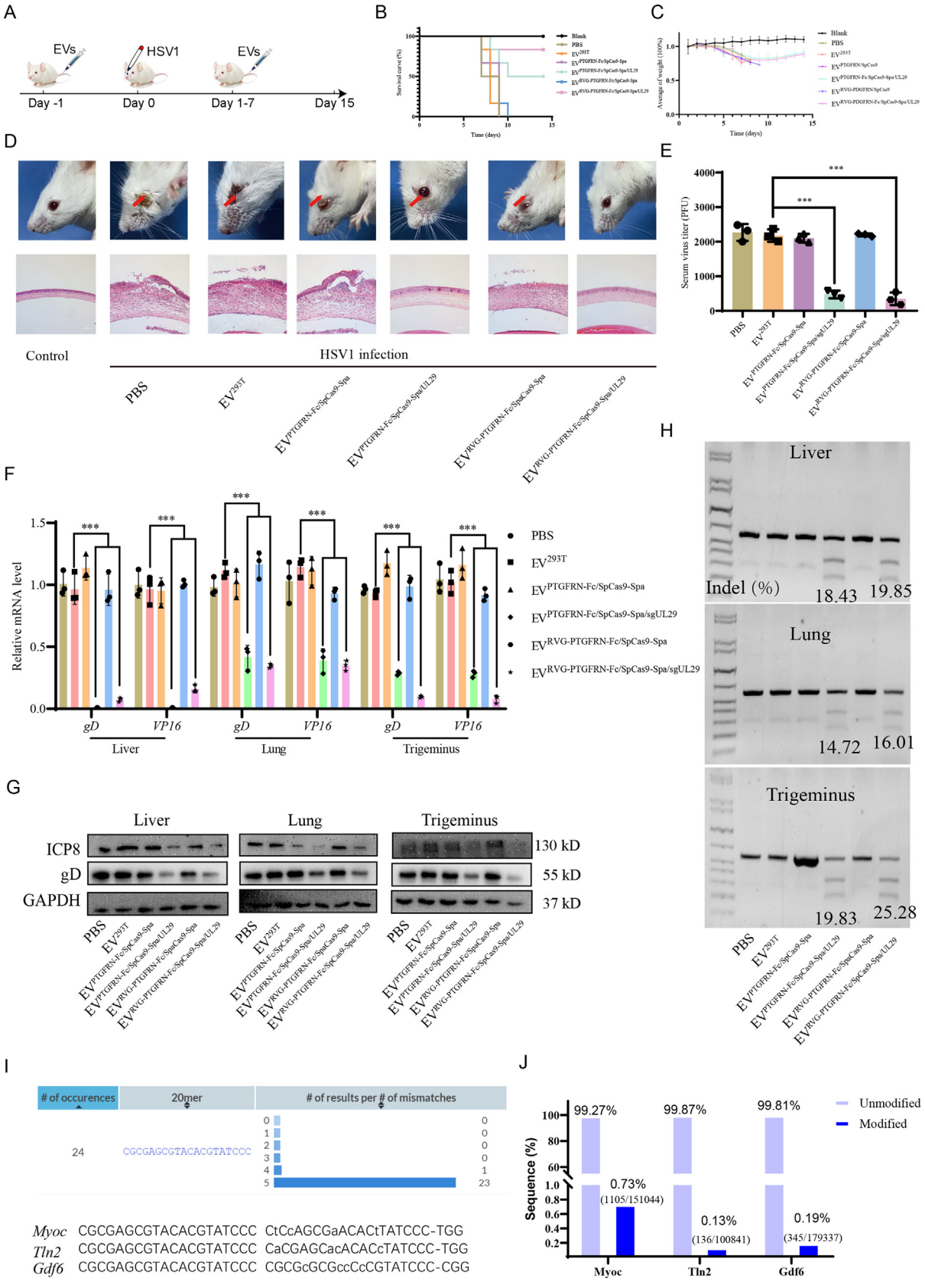

Figure 6 The anti-HSV-1 activity of EVs *in vivo*. (A) Schematic illustration of EVs (1×10^{10} vesicles) for *in vivo* delivery for the treatment of HSV-1 infection. (B) Survival rates and (C) body weight of mice after the specified treatments. Statistical significance was calculated by log-rank test (Means ± SD, $n = 6$). (D) Morphological change and HE stain of the eyeball in mice during the experiment. (E) The virus titration of mouse

packaging, 41.35 ng *vs* 9.86 ng (Fig. 3C). The quantification of EV protein content revealed that SpCas9 constituted approximately 1% of the total protein packaged in $EV^{PTGFRN-Fc/SpCas9-Spa}$ (Supporting Information Fig. S3).

To distinguish whether the encapsulation of SpCas9/sgRNA complex inside EVs was facilitated by the binding of PTGFRN-Fc and SpCas9-Spa or if it was solely attached to the surface of the isolated EVs, we conducted proteinase K protection assays to isolated from 293T cells were treated with proteinase K with/without Triton X-100. When exposed to proteinase K without detergent, SpCas9 remained intact. However, when Triton X-100 was present, SpCas9 underwent degradation while the membrane protein CD9 was not changed (Fig. 3D). This suggested that SpCas9 was enclosed within EVs (Fig. 3D). To better understand the retention time of EVs carrying SpCas9, we conducted a thorough investigation. Our analysis revealed that the delivery of SpCas9 reached its highest level after 12 h and then gradually decreased over time. After 48 h, the level of SpCas9 became undetectable when analyzed through Western blotting (Fig. 3E).

Next, we assessed the packaging efficacy of sgRNA designed to target EGFP by $EV^{PTGFRN-Fc/SpCas9-Spa}$. By extracting sgRNA from these EVs, RT-qPCR was used to detect the content of sgRNA. The data indicated the content of sgRNA-EGFP level in $EV^{PTGFRN-Fc/SpCas9-Spa}$ were approximately 10-fold higher than in $EV^{PTGFRN-Fc/SpCas9}$ (Fig. 3F), the DNA-gel showed the same results, suggesting that the encapsulation of SpCas9 favors sgRNA encapsulation as well. The sgRNA-EGFP sequence in EVs was cloned to the T vector and confirmed by Sanger sequencing (Fig. 3G). Moreover, the green fluorescence signal in EGFP-stable expressing 293T cells was decreased by 70% with $EV^{PTGFRN-Fc/SpCas9-Spa/sgEGFP}$ treatment compared with that of $EV^{PTGFRN-Fc/SpCas9/sgEGFP}$ treatment under microscope (Fig. 3H) and flow cytometry (Fig. 3I and Fig. S2C). Collectively, these data provided solid evidence that the Fc/Spa system efficiently promoted the encapsulation of SpCas9/sgRNA RNP into EVs.

3.3. *Cas9/sgRNA-RNP delivered by* $EV^{PTGFRN-Fc/Cas9-Spa}$ *alleviates HSV1 infection*

Considering the remarkable properties of the Fc/Spa systems in the packaging of Cas9 into EVs, we decided to evaluate its efficacy in combatting viral infections. HSV1 is a common DNA virus, and $EV^{PTGFRN-Fc/SpCas9-Spa}$ could be a potentially effective way to eradicate the HSV1 genome. First, we applied two sgRNAs against two crucial viral genes, the glycoprotein UL8 and single-stranded DNA binding protein UL29 (alternate name: ICP8) based on previous study[26] (Fig. 4A). *In vitro* transfection of plasmids containing sgUL8-spCas9 or sgUL29-spCas9 displayed promising antiviral effects by reducing cell cytopathic effects (CPE) (Supporting Information Fig. S4A). The targeting efficiency of UL8 and UL29 in disrupting the endogenous gene was confirmed by analyzing the frequencies of indel mutations using a T7E1 cleavage assay. The results showed a mutation frequency of 21.71% for UL29 and 3.25% for UL8 (Fig. 4B). The TIDE analysis indicated similar indel rates of about 18.2% for UL29 (Fig. S4B). Due to the high indel rates of UL29, we thus packed UL29-sgRNA with SpCas9 into the engineering EVs in the following study.

After transfecting the relevant plasmids into 293T cells, the resulting EVs were assessed for their efficacy in combating HSV1 infection in Vero cells. EV^{293T}, $EV^{PTGFRN-Fc/SpCas9}$, $EV^{PTGFRN-Fc/SpCas9-Spa}$, were added to EV-free medium after the cells were infected with demonstrated a noteworthy reduction in virus-induced cytopathy compared to other treatment groups in Vero cells (Fig. 4C). Compared with $EV^{PTGFRN-Fc/SpCas9/sgUL29}$, the advantage of $EV^{PTGFRN-Fc/SpCas9-Spa/sgUL29}$ in reducing ICP8 protein could be easily observed, which also inhibited viral gD protein by Western blotting (Fig. 4D) and RT-qPCR (Fig. 4E). The antiviral efficacy of $EV^{PTGFRN-Fc/SpCas9-Spa/sgUL29}$ was validated through viral plaque formation assays, the histogram indicated a quantification of the viral plaque showing up to a 90% reduction in the number of progeny plaque formations (Fig. 4F). The endogenous targeted disruption efficiency was evaluated by T7EI assay, which clearly indicated about 17.86% indel frequencies after $EV^{PTGFRN-Fc/SpCas9-Spa/sgUL29}$ treatment, compared to 11.01% with $EV^{PTGFRN-Fc/SpCas9/sgUL29}$ treatment (Fig. 4G), indicating that the indel efficiency was increased about 62% compared to $EV^{PTGFRN-Fc/SpCas9/sgUL29}$. To test whether EVs activate the type I IFN-dependent innate immune response, we detected the TBK1 phosphorylation and found that EVs did not provoke innate immune activation against HSV1 infection (Fig. S4C). Together, these data suggested that $EV^{PTGFRN-Fc/SpCas9-Spa/sgUL29}$ inhibited HSV1 infection through SpCas9-based DNA editing rather than relying on a type I IFN-related innate immune response.

3.4. *RVG decoration mediated neuro-targeting of EVs delivery*

Given that nervous tissue is particularly susceptible to HSV1 invasion, we aimed to develop EVs containing a neuro-targeting peptide known as rabies virus glycoprotein peptide (RVG29), which has strong neuro-targeting tropism[27]. This is intended to eliminate the HSV1 virus within nervous tissue. RVG29 was fused to the extracellular domain of PTGFRN-Δ687 with an HA tag, and the IP results confirmed the outside display of RVG-decorated EVs successfully, named $EV^{RVG-PTGFRN-Fc/SpCas9-Spa/sgUL29}$ (Fig. 5A and B). To further verify whether the RVG modification affects the original anti-HSV1 activity, $EV^{RVG-PTGFRN-Fc/SpCas9-Spa/sgUL29}$ was added into HSV1-infected Hela cells. The T7E1 assay indicated no difference between the $EV^{PTGFRN-Fc/SpCas9-Spa/sgUL29}$ and $EV^{RVG-PTGFRN-Fc/SpCas9-Spa/sgUL29}$, the indel rates were 16.98% and 18.11%, respectively, by TIDE analyze (Fig. 5C). In addition, the antiviral ability was similar between the treatment of $EV^{PTGFRN-Fc/SpCas9-Spa/sgUL29}$ and $EV^{RVG-PTGFRN-Fc/SpCas9-Spa/sgUL29}$, indicated by viral gD protein and HSV1 ICP8 protein *via* Western blotting assay (Fig. 5D). These data suggested that modification of RVG did not change the antiviral activity of $EV^{RVG-PTGFRN-Fc/SpCas9-Spa/sgUL29}$.

To examine its neuro-targeting efficiency, neuro HT22 cells were exposed to Dil-labelled $EV^{RVG-PTGFRN-Fc/SpCas9-Spa/sgUL29}$ and $EV^{PTGFRN-Fc/SpCas9-Spa/sgUL29}$. Compared to the Hela cells,

serum by plaque formation assay. Vero cells were plated in 24-well plates at 2×10^5 cells/mL and cultured for 24 h. The serum was added to the cells after 10-fold dilution with blank DMEM medium and incubated at 37 °C for 1 h. Finally, DMEM solid medium was used for culture for 72 h. (F and G) The viral gene and protein levels were analyzed by RT-qPCR (F) and Western blotting (G). (H) Analysis of gene editing efficiency in liver, lung, and trigeminal nerve by T7EI. (I) Prediction of off-target genes. (J) The off-targets efficacy by deep sequencing analysis. Data were presented as mean ± SD ($n = 6$, $^{***}P < 0.001$).

the cell uptake efficiency was increased in HT22 cells, indicated by the red fluorescence signal under a confocal microscope (Fig. 5E and F), supporting a good neuro-targeting ability of RVG-decorated EV. We then evaluated the ability of the EVs to traverse the vascular endothelial cell targeting neuro cells through Transwell assay. Endothelial cells (HUVECs) were seeded to the up cavity, then $EV^{PTGFRN-Fc/SpCas9-Spa/sgUL29}$ or $EV^{RVG-PDGFRN-Fc/SpCas9-Spa/sgUL29}$ stained with Dil was added into the up medium (Fig. 5G). Compared to $EV^{PTGFRN-Fc/SpCas9-Spa/sgUL29}$, the results indicated $EV^{RVG-PTGFRN-Fc/SpCas9-Spa/sgUL29}$ passed through the endothelial cells and entered the underlying HT22 cell, indicated by the red fluorescence signal that represented all the red fluorescence in the picture (Fig. 5G and H).

In pharmacokinetic studies, the distribution and organ accumulation were assessed by *ex vivo* organ fluorescence in BALB/c mice followed by intravenously injecting with Dil-labelled EV^{293T}, $EV^{PTGFRN-Fc/SpCas9-Spa/sgUL29}$ and $EV^{RVG-PTGFRN-Fc/SpCas9-Spa/sgUL29}$ (10^{10} particles/mice). Quantitation of fluorescence in the organs showed that the brain accumulation of $EV^{RVG-PTGFRN-Fc/SpCas9-Spa/sgUL29}$, which further indicates the neuro-targeting of $EV^{RVG-PTGFRN-Fc/SpCas9-Spa/sgUL29}$ (Fig. 5I). Quantitative results for other organs were shown in Fig. S4D. In a word, this study indicated that the RVG decoration-mediated neuro-targeting increased the accumulation of EVs in the neuro-enriched brain tissue.

3.5. *The pharmacokinetics and safety study of* $EV^{RVG-PTGFRN-Fc/SpCas9-Spa/sgUL29}$

To study the pharmacokinetics of engineered EVs, we then detected EVs concentration in mice plasma at different time points after tail vein injection of EV^{293T}, $EV^{PTGFRN-Fc/SpCas9-Spa/sgUL29}$ and $EV^{RVG-PTGFRN-Fc/SpCas9-Spa/sgUL29}$ labelled with Dil (Fig. S4E). The maximal fluorescence signal and half-life of EVs in plasma were similar among EV^{293T}, $EV^{PTGFRN-Fc/SpCas9-Spa/sgUL29}$, and $EV^{RVG-PTGFRN-Fc/SpCas9-Spa/sgUL29}$, and these EVs went through elimination time with a half-life about 12 h (Fig. S4E). These results indicated that the *in vivo* pharmacokinetics of the engineered EVs were consistent with those of the natural EVs. Next, we detected the potential toxicity of EVs. The effect of EVs on cell viability was investigated by CCK-8 *in vitro*. The results displayed low cytotoxicity and hardly affected the cell viability of engineered EVs in three widely used cell lines (Supporting Information Fig. S5A). We also evaluated the biocompatibility and the safety of EVs *in vivo*. The healthy BALB/c mice were treated with EV^{293T}, $EV^{PTGFRN-Fc/SpCas9-Spa/sgUL29}$, $EV^{RVG-PTGFRN-Fc/SpCas9-Spa/sgUL29}$. After 8 consecutive days of EV administration, we continued to observe the status of the mice until the 20th day. During the treatment period, we found no significant loss in body weight for these days (Fig. S5B). HE stain of major organs further revealed that there were no obvious pathological changes after the repeated administration of EVs (Fig. S5C), as compared with control mice. Additionally, on the 20th day, we conducted an open field test (Supporting Information Fig. S6A–C), novel object recognition test (Fig. S6D and E), and rotarod test (Fig. S6F) to investigate the behaviour of the mice after EVs administration[19,28]. Compared with the PBS group, there were no obvious changes in the EVs administration group, and these findings suggested that the administration of the engineered EVs is safe for mice perceiving and behaving. To address concerns regarding the potential immunogenicity of the RVG peptide, we detected the presence of antibodies to the RVG. No significant differences were observed in the immune response between these groups (Fig. S6G). The small size of the peptides (only 29 aa) renders them non-immunogenic. In brief, these results demonstrated that the administration of EVs for a short duration of 8 consecutive days exhibited a significant level of safety in mice.

3.6. *The antiviral ability of* $EV^{RVG-PTGFRN-Fc/SpCas9-Spa/sgUL29}$ *in vivo*

In consideration of the safety measures for electric vehicle production, we conducted a study on the *in vivo* antiviral efficacy of modified EVs against HSV1. We used a BALB/c mouse intranasal inoculation model of HSV1 as previously described[9–11,18,29]. EV^{293T}, $EV^{PTGFRN-Fc/SpCas9-Spa}$, $EV^{PTGFRN-Fc/SpCas9-Spa/sgUL29}$ were administrated by tail vein injection 1 day before HSV1 infection (Fig. 6A) due to the strategy of pre-administering EVs to saturate the macrophage system[30]. This approach aimed to reduce the subsequent EV phagocytosis. Accordingly, we adopted this strategy in our study. Morphology results indicated the EVs were in good condition (Supporting Information Fig. S7A). Then, EVs injection lasted 7 days after viral infection with 100 μL/day/mice, which contained 3×10^9 particles (Fig. 6A). From the mice survival rates, all mice were sacrificed on the 15th day with EV^{293T} treatment after HSV1 infection. However, the survival rate of mice reached 60% with $EV^{PTGFRN-Fc/SpCas9-Spa/sgUL29}$ treatment. After administration of $EV^{RVG-PTGFRN-Fc/SpCas9-Spa/sgUL29}$, the survival rate of mice reached 80% (Fig. 6B). In addition, the body weight of the mice continued to decline after HSV1 infection and slowly increased on Day 10. Mice given $EV^{RVG-PTGFRN-Fc/SpCas9-Spa/sgUL29}$ regained more body weight than those given $EV^{PTGFRN-Fc/SpCas9-Spa/sgUL29}$ (Fig. 6C). HSV1 could travel along the nerve in nose after intranasal inoculation, enter the eye and cause damage to the cornea, so we could observe lesions in the eye easily. In mice treated with EV^{293T}, HSV1 induced obvious edema in the eyeballs with hypercellularity of the sclera and detachment of the retina from overall view after administration (Fig. 6D). In contrast, mice treatment with $EV^{PTGFRN-Fc/SpCas9-Spa/sgUL29}$ displayed moderate edema in the eyeballs. We also did a pathological assay and found that the $EV^{PTGFRN-Fc/SpCas9-Spa/sgUL29}$ or $EV^{RVG-PTGFRN-Fc/SpCas9-Spa/sgUL29}$ treatment did significantly improve the corneal pathology (Fig. 6D).

Next, the viral titer levels in serum were analyzed. After administration of $EV^{PTGFRN-Fc/SpCas9-Spa/sgUL29}$, the viral titration in serum was significantly reduced compared to other groups (Fig. 6E). The viral gene transcriptional levels were analyzed by RT-qPCR in the lung, liver and trigeminal nerve. The viral protein transcriptional level was similar between $EV^{RVG-PTGFRN-Fc/SpCas9-Spa/sgUL29}$ and $EV^{PTGFRN-Fc/SpCas9-Spa/sgUL29}$ treatment group in the lung and liver. However, the viral protein transcriptional level (*gD* and *VP16*) was largely reduced in the $EV^{RVG-PTGFRN-Fc/SpCas9-Spa/sgUL29}$ treatment group than in $EV^{PTGFRN-Fc/SpCas9-Spa/sgUL29}$ treatment group in trigeminal nerve (Fig. 6F). Similar results were also observed in viral protein level (Fig. 6G).

HSV genome editing efficiency was analyzed by T7EI analysis in mouse lung and trigeminal nerve separately. In lung tissue, we observed similar indel efficiencies after $EV^{RVG-PTGFRN-Fc/SpCas9-Spa/sgUL29}$ and $EV^{PTGFRN-Fc/SpCas9-Spa/sgUL29}$ treatment (14.72% *vs* 16.01%). However, in the trigeminal nerve, the indel mutation after $EV^{RVG-PTGFRN-Fc/SpCas9-Spa/sgUL29}$ treatment was treatment (19.83% *vs* 25.28%) (Fig. 6H). Three top mismatch predicted off-target genes from Off-Spotter were analyzed by deep sequencing to determine the off-target effects on the mouse genome, *Myoc*, *Tln2*, and *Gdf6* (Fig. 6I). The data indicated a low gene indel

rate in trigeminal nerve with $EV^{PTGFRN-Fc/SpCas9-Spa/sgUL29}$ treatment, *Myoc* (0.73%), *Tln2* (0.13%) and *Gdf6* (0.19%) (Fig. 6J and Fig. S7B).

4. Discussion

The establishment of CRISPR/Cas9 technology for eukaryotic gene editing opened up new avenues not only for the analysis of gene function but also for therapeutic interventions[31,32]. However, the viral delivery system leads to the increase of off-target editing and viral vector integration into the genome of transduced cells[33]. Therefore, EVs are a natural ideal carrier that can address the issue of virus carrier[1], Our and other groups have previously reported several CRISPR-RNP delivery systems utilizing the cellular packaging machinery for inserting cargo into EVs, such as Com/com system, chemical-induced FKBP12 and FRB dimerization system[34], protein myristoylation system[35], gesicles system[36], genome editing with designed extracellular vesicles system[37]. At the same time, it's still urgent to develop novel delivery systems to meet diverse clinical needs. In this study, we first introduced the Fc/Spa protein interaction system into the engineering EVs for the CRISPR/Cas9 RNP package, which is an active enrichment of RNP in EVs and is an appealing approach for efficient CRISPR/Cas9 genome editing. Compared with other CRISPR-RNP cellular packaging strategies, the Fc/Spa system has two significant advantages. One is the interaction between Fc and Spa is strong, which recruits about two folds of spCas9 into the engineering EVs. This innovative approach enhances the ease and effectiveness of the enrichment process. The other advantage is the interaction between Fc and Spa could be easily dissociated in an acidic environment of lysosomal during the endocytosis of EVs into cells, which is helpful for the subsequent SpCas9 lysosomal escape process. We also confirmed the role of VSV-G in the escape of the RNPs from the endosome system in recipient cells. Combined with the VSV-G proteins, we observed significant EVs escaping from lysosomes into the cytoplasm. These phenomena indicated the Fc/Spa's ability to actively recruit cargo into EVs. In addition, this model could be readily applied to other CRISPR systems for delivery purposes without the need to modify the structural region of the sgRNA. This eliminates the potential risk of reducing the activity of the CRISPR system. These advantages highlight the versatility and practicality of our model in various gene-editing applications.

Another important finding was that surface modification of EVs with PTGFRN-Fc showed good cargo packaging ability, which is consistent with the previous report[4]. Cre could be efficiently packaged into EVs by Fc/Spa. Also, Cre protein could be released into the cells intact to turn the cell from red to green fluorescence signal. Besides Cre, SpCas9 could be packaged into the EVs. Our data indicated Fc/Spa packaged 41.1 ng of SpCas9 into EVs, two fold more SpCas9 relative to systems without Fc/Spa tagged versions. Our previous work has shown that SpCas9 protein has a short lifespan (12 h) in recipient cells. This study indicated that SpCas9 protein levels were highest within 8 h and decreased by 24 h in recipient cells. These phenomena coincided with the time when EVs entered the cell. EVs were first attached to the cell surface within 1 h. At 8 h, EVs completely entered the cell, but lysosomes degraded them after 24 h incubation. The median size of EVs derived from the EV-producing cells was around ~150 nm, which was similar to the EVs incorporated with Fc/Spa. We found that the size of the EVs was not affected by how much it was loaded. Besides the size, the Zeta potentials, shape, as well as marker proteins of Fc/Spa-engineered EVs were not affected. At the same time, we also observed the synchronous rise of the corresponding sgRNA in EVs, suggesting that the enrichment of SpCas9 can also promote the packaging of sgRNA. Since our previous studies and others' studies confirmed that the design of cytoplasmic sgRNA could not increase the sgRNA content in EVs[6,34], such as RNA polymerase II promoter-driven sgRNA or ribozyme modified sgRNA, we thus did not apply this strategy in this study.

Following acute infection, HSV establishes latency in sensory neurons, from which it can reactivate and cause recurrent disease. Available antiviral therapies do not affect latent viral genomes; therefore, they do not prevent reactivation following therapy cessation[38]. One possible curative approach involves the introduction of DNA double-strand breaks in latent HSV genomes by rare-cutting endonucleases, leading to mutagenesis of essential viral genes[39–41]. For this purpose, UL29 was chosen for gene editing, which was essential for viral proliferation, and used in replication-defective vaccines with UL29 deleted. RVG (29 aa) was fused to the extracellular domain of PTGFRN-Δ687, which prepared the neural targeting EVs[27]. Several studies have also employed this strategy to deliver siRNA into the brain for the treatment of Zika virus infection[42]. We showed this engineering EVs could enter the brain through the blood–brain barrier (BBB) and have therapeutic efficacy *in vitro* and *in vivo* models. Considering the issue that RVG modification does not show comparable neuro-targeting efficiency *in vivo* as *in vitro*, we hypothesize that two factors may contribute to the slightly weaker *in vivo* efficacy compared to the *in vitro* results. Firstly, the presence of the BBB is likely to reduce the EVs entering the trigeminal nerve, thereby diminishing their effectiveness. Secondly, the phagocytic activity of macrophages in the body can significantly impact EVs, as macrophage cells tend to phagocytose EVs. Despite our attempts to reduce the endocytosis of macrophages through the pre-administration of EV treatment, endocytosis of macrophage activity still influences the outcome of EVs. Taking these factors into consideration, the *in vitro* results surpass the *in vivo* experiments. However, this understanding provides valuable insights for further optimizing our system. Another limitation of this study is the need for pharmacokinetics of EVs. Evaluating such macromolecules is still challenging and needs further investigation.

Based on metabolism experiments of EVs in 293T cells, we administered a once-a-day dose to mice. The engineered EV system showed a good safety ability from the *in vivo* safety results, non-toxic to cells, no change in body weight, and no lesions in the organs. In terms of antiviral effects *in vivo*, $EV^{RVG-PTGFRN-Fc/SpCas9-Spa/UL29}$ showed a significant effect in preventing the death of HSV1-infected mice. Especially in trigeminal nerve, $EV^{RVG-PTGFRN-Fc/SpCas9-Spa/sgUL29}$ showed a better gene-editing effect than $EV^{PTGFRN-Fc/SpCas9-Spa/sgUL29}$ by T7EI, suggesting $EV^{RVG-PTGFRN-Fc/SpCas9-Spa/sgUL29}$ is capable of modulating the HSV1 reservoir in the trigeminal nerve with less off-target effects. Taken together, our study supports the engineering of EVs to deliver CRISPR-cas9 for treating HSV infection.

Acknowledgments

This study was supported by the Guangdong Basic and Applied Basic Research Foundation (2023A1515030057, Xingang Yao) and the National Natural Science Foundation of China (82373873,

Xingang Yao). We also thank Professor Haitao Wang and Yingying Fang's help and suggestion on the mouse behaviour experiments.

Author contributions

Xingang Yao, Shuwen Liu, and Wenyu Wu conceived and designed the project; Yuanda Wan, Liren Li, and Ruilin Chen conducted experiments; Yuanda Wan, Jiajia Han, Qiyun Lei, Xiaodong Tang, Zhipeng Chen performed data analysis and discussion; Yuanda Wan, Xingang Yao wrote the manuscript.

Conflicts of interest

The authors declare no conflicts of interest.

Appendix A. Supporting information

Supporting data to this article can be found online at https://doi.org/10.1016/j.apsb.2023.10.004.

References

1. Cheng L, Hill AF. Therapeutically harnessing extracellular vesicles. *Nat Rev Drug Discov* 2022;**21**:379−99.
2. Buzas EI. The roles of extracellular vesicles in the immune system. *Nat Rev Immunol* 2022;**23**:236−50.
3. Zhang S, Shen JT, Li DL, Cheng YY. Strategies in the delivery of Cas9 ribonucleoprotein for CRISPR/Cas9 genome editing. *Theranostics* 2021;**11**:614−48.
4. Dooley K, McConnell RE, Xu K, Lewis ND, Haupt S, Youniss MR, et al. A versatile platform for generating engineered extracellular vesicles with defined therapeutic properties. *Mol Ther* 2021;**29**:1729−43.
5. Hung ME, Leonard JN. A platform for actively loading cargo RNA to elucidate limiting steps in EV-mediated delivery. *J Extracell Vesicles* 2016;**5**:31027.
6. Yao XG, Lyu P, Yoo K, Yadav MK, Singh R, Atala A, et al. Engineered extracellular vesicles as versatile ribonucleoprotein delivery vehicles for efficient and safe CRISPR genome editing. *J Extracell Vesicles* 2021;**10**:e12076.
7. Braisted AC, Wells JA. Minimizing a binding domain from protein A. *Proc Natl Acad Sci U S A* 1996;**93**:5688−92.
8. McCormick I, James C, Welton NJ, Mayaud P, Turner KME, Gottlieb SL, et al. Incidence of herpes simplex virus keratitis and other ocular disease: global review and estimates. *Ophthalmic Epidemiol* 2022;**29**:353−62.
9. Aubert M, Madden EA, Loprieno M, DeSilva Feelixge HS, Stensland L, Huang ML, et al. *In vivo* disruption of latent HSV by designer endonuclease therapy. *JCI Insight* 2016;**1**:e88468.
10. Aubert M, Strongin DE, Roychoudhury P, Loprieno MA, Haick AK, Klouser LM, et al. Gene editing and elimination of latent herpes simplex virus *in vivo*. *Nat Commun* 2020;**11**:4148.
11. Yin D, Ling SK, Wang DW, Dai Y, Jiang H, Zhou XJ, et al. Targeting herpes simplex virus with CRISPR-Cas9 cures herpetic stromal keratitis in mice. *Nat Biotechnol* 2021;**39**:567−77.
12. Stringer BW, Day BW, D'Souza RCJ, Jamieson PR, Ensbey KS, Bruce ZC, et al. A reference collection of patient-derived cell line and xenograft models of proneural, classical and mesenchymal glioblastoma. *Sci Rep* 2019;**9**:4902.
13. Clement K, Rees H, Canver MC, Gehrke JM, Farouni R, Hsu JY, et al. CRISPResso2 provides accurate and rapid genome editing sequence analysis. *Nat Biotechnol* 2019;**37**:224−6.
14. Wan YH, Wu SG, Zheng SC, Liang E, Liu SW, Yao XG, et al. A series of octahydroquinazoline-5-ones as novel inhibitors against dengue virus. *Eur J Med Chem* 2020;**200**:112318.
15. Wan YH, Wu WY, Guo SX, He SJ, Tang XD, Wu XY, et al. [1,2,4] Triazolo[1,5-a]pyrimidine derivative (Mol-5) is a new NS5-RdRp inhibitor of DENV2 proliferation and DENV2-induced inflammation. *Acta Pharmacol Sin* 2020;**41**:706−18.
16. Wan YH, Wu WY, Wan YD, Li LR, Zhang JW, Chen XG, et al. Brivanib alaninate inhibited dengue virus proliferation through VEGFR2/AMPK pathway. *Pharmacol Res* 2021;**170**:105721.
17. Chen WH, Zhang JW, Qi X, Zhao K, Pang XY, Lin XP, et al. *p*-Terphenyls as anti-HSV-1/2 agents from a deep-sea-derived penicillium sp. *J Nat Prod* 2021;**84**:2822−31.
18. Pegg CE, Zaichick SV, Bomba-Warczak E, Jovasevic V, Kim D, Kharkwal H, et al. Herpesviruses assimilate kinesin to produce motorized viral particles. *Nature* 2021;**599**:662−6.
19. Guo HB, Cheng YF, Wu JG, Wang CM, Wang HT, Zhang C, et al. Donepezil improves learning and memory deficits in APP/PS1 mice by inhibition of microglial activation. *Neuroscience* 2015;**290**:530−42.
20. Myskiw JC, Rossato JI, Bevilaqua LR, Medina JH, Izquierdo I, Cammarota M. On the participation of mTOR in recognition memory. *Neurobiol Learn Mem* 2008;**89**:338−51.
21. Yan YQ, Zheng R, Liu Y, Ruan Y, Lin ZH, Xue NJ, et al. Parkin regulates microglial NLRP3 and represses neurodegeneration in Parkinson's disease. *Aging Cell* 2023;**22**:e13834.
22. McConnell RE, Youniss M, Gnanasambandam B, Shah P, Zhang W, Finn JD. Transfection reagent artefact likely accounts for some reports of extracellular vesicle function. *J Extracell Vesicles* 2022;**11**:e12253.
23. Witwer KW, Soekmadji C, Hill AF, Wauben MH, Buzas EI, Di Vizio D, et al. Updating the MISEV minimal requirements for extracellular vesicle studies: building bridges to reproducibility. *J Extracell Vesicles* 2017;**6**:1396823.
24. Florkiewicz RZ, Rose JK. A cell line expressing vesicular stomatitis virus glycoprotein fuses at low pH. *Science* 1984;**225**:721−3.
25. Riedel H, Kondor-Koch C, Garoff H. Cell surface expression of fusogenic vesicular stomatitis virus G protein from cloned cDNA. *EMBO J* 1984;**3**:1477−83.
26. Muylaert I, Tang KW, Elias P. Replication and recombination of herpes simplex virus DNA. *J Biol Chem* 2011;**286**:15619−24.
27. Kumar P, Wu H, McBride JL, Jung KE, Kim MH, Davidson BL, et al. Transvascular delivery of small interfering RNA to the central nervous system. *Nature* 2007;**448**:39−43.
28. Qiu ZK, Zhang LM, Zhao N, Chen HX, Zhang YZ, Liu YQ, et al. Repeated administration of AC-5216, a ligand for the 18 kDa translocator protein, improves behavioral deficits in a mouse model of post-traumatic stress disorder. *Prog Neuro-Psychopharmacol Biol Psychiatry* 2013;**45**:40−6.
29. Bohannon KP, Sollars PJ, Pickard GE, Smith GA. Fusion of a fluorescent protein to the pUL25 minor capsid protein of pseudorabies virus allows live-cell capsid imaging with negligible impact on infection. *J Gen Virol* 2012;**93**:124−9.
30. Belhadj Z, He B, Deng HL, Song SY, Zhang H, Wang XQ, et al. A combined "eat me/don't eat me" strategy based on extracellular vesicles for anticancer nanomedicine. *J Extracell Vesicles* 2020;**9**:1806444.
31. Shivram H, Cress BF, Knott GJ, Doudna JA. Controlling and enhancing CRISPR systems. *Nat Chem Biol* 2021;**17**:10−9.
32. Raguram A, Banskota S, Liu DR. Therapeutic *in vivo* delivery of gene editing agents. *Cell* 2022;**185**:2806−27.
33. Lino CA, Harper JC, Carney JP, Timlin JA. Delivering CRISPR: a review of the challenges and approaches. *Drug Deliv* 2018;**25**:1234−57.
34. Gee P, Lung MSY, Okuzaki Y, Sasakawa N, Iguchi T, Makita Y, et al. Extracellular nanovesicles for packaging of CRISPR-Cas9 protein and sgRNA to induce therapeutic exon skipping. *Nat Commun* 2020;**11**:1334.

35. Whitley JA, Kim S, Lou L, Ye C, Alsaidan OA, Sulejmani E, et al. Encapsulating Cas9 into extracellular vesicles by protein myristoylation. *J Extracell Vesicles* 2022;**11**:e12196.
36. Campbell LA, Coke LM, Richie CT, Fortuno LV, Park AY, Harvey BK. Gesicle-mediated delivery of CRISPR/Cas9 ribonucleoprotein complex for inactivating the HIV provirus. *Mol Ther* 2019;**27**:151−63.
37. Lainscek D, Kadunc L, Keber MM, Bratkovic IH, Romih R, Jerala R. Delivery of an artificial transcription regulator dCas9-VPR by extracellular vesicles for therapeutic gene activation. *ACS Synth Biol* 2018;**7**:2715−25.
38. Klysik K, Pietraszek A, Karewicz A, Nowakowska M. Acyclovir in the treatment of herpes viruses - a review. *Curr Med Chem* 2020;**27**:4118−37.
39. Bommareddy PK, Peters C, Kaufman HL. Generation and validation of recombinant herpes simplex type 1 viruses (HSV-1) using CRISPR/Cas9 genetic disruption. *Methods Enzymol* 2020;**635**:167−84.
40. Ni LQ, Li Y, Wu K, Deng F, Wang HL, Ning YJ. Antitumor efficacy of CRISPR/Cas9-engineered ICP6 mutant herpes simplex viruses in a mouse xenograft model for lung adenocarcinoma. *J Med Virol* 2022;**94**:6000−15.
41. Russell TA, Stefanovic T, Tscharke DC. Engineering herpes simplex viruses by infection-transfection methods including recombination site targeting by CRISPR/Cas9 nucleases. *J Virol Methods* 2015;**213**:18−25.
42. Zhang R, Fu YX, Cheng M, Ma WY, Zheng N, Wang YX, et al. sEVs(RVG) selectively delivers antiviral siRNA to fetus brain, inhibits ZIKV infection and mitigates ZIKV-induced microcephaly in mouse model. *Mol Ther* 2022;**30**:2078−91.